Kilohertz gravitational waves from binary neutron star mergers: Numerical-relativity informed postmerger model

Matteo Breschi,[1] Sebastiano Bernuzzi,[1] Kabir Chakravarti,[1] Alessandro Camilletti,[2,3] Aviral Prakash,[4,5] and Albino Perego[2,3]

[1]*Theoretisch-Physikalisches Institut, Friedrich-Schiller-Universität Jena, 07743, Jena, Germany*
[2]*Dipartimento di Fisica, Università di Trento, Via Sommarive 14, 38123 Trento, Italy*
[3]*INFN-TIFPA, Trento Institute for Fundamental Physics and Applications, via Sommarive 14, I-38123 Trento, Italy*
[4]*Institute for Gravitation and the Cosmos, The Pennsylvania State University, University Park, Pennsylvania 16802, USA*
[5]*Department of Physics, The Pennsylvania State University, University Park, Pennsylvania 16802, USA*

(Received 23 May 2022; accepted 15 November 2022; published 4 March 2024)

We present NRPMw, an analytical model of gravitational-waves from neutron star merger remnants informed using 618 numerical relativity (NR) simulations. NRPMw is designed in the frequency domain using a combination of complex Gaussian wavelets. The wavelet's parameters are calibrated to equations of state (EOSs) insensitive relations from NR data. The NR simulations are computed with 21 EOSs (seven of which are finite-temperature microphysical models, and three of which contain quark phase transitions or hyperonic degrees of freedom) and span total binary masses $M \in [2.4, 3.4] M_\odot$, mass ratios up to $q = 2$, and (nonprecessing) dimensionless spins magnitudes up to 0.2. The theoretical uncertainties of the EOS-insensitive relations are incorporated in NRPMw using recalibration parameters that enhance the flexibility and accuracy of the model. NRPMw is NR faithful with fitting factors $\gtrsim 0.9$ computed on an independent validation set of 102 simulations.

DOI: 10.1103/PhysRevD.109.064009

I. INTRODUCTION

This work is the first of a series of papers that present a faithful and complete (inspiral-merger-postmerger) model for gravitational-wave (GW) signals from binary neutron star (BNS) mergers, and its application to GW analyses with the third-generation Einstein Telescope (ET) detector [1–5]. Our model builds on a state-of-art effective-one-body (EOB) approach for the inspiral-merger regime [6–9] and on its numerical relativity (NR) completion for the remnant's emission [10,11]. Prospects applications to ET GW observations include the following: the precision measurement of the neutron star (NS) tidal polarizability parameters [12,13], the determination of the remnant's black hole (BH) collapse [14,15], constraints on the extreme density equation of state (EOS) [16,17], and multimessenger observations [18]. These case studies will be further discussed in companion papers in the context of a Bayesian analysis framework [19] (paper II hereafter). Here, we start presenting NRPMw, a new analytical model for the postmerger (PM) emission from merger's remnant, that improves over our previous NRPM [11].

The PM GW emission from a merger's remnant is predicted to have a peak luminosity at frequencies of few kilohertz, e.g. [11,20–24]. This high-frequency GW transient can be robustly computed by means of NR simulations and it is key to directly probe the nature of the remnant in a (possibly multimessenger) BNS merger observation. A GW observation from a merger remnant is also a promising probe for the nuclear EOS at extreme densities, e.g. [16,17,25–27]. Kilohertz PM transients are unlikely to be captured by current ground-based detectors [28], and no PM signal was detected for GW170817 [29–32]. However, they are a main target for third-generation observatories [2,5,33–35] and for finely tuned instruments [36]. In view of these considerations, it is essential to develop accurate PM models for Bayesian GW analyses.

Models of PM GWs were presented in Refs. [11,21,22,37–45]. These templates are phenomenological models that capture the main PM spectral features but do not attempt to model the underlining remnant's dynamics. The complex spectral frequencies are either inferred from the observations or (in part) fixed by EOS-insensitive (quasiuniversal) relations that connect the main spectral features to the binary parameters. Depending on whether the quasiuniversal relations are employed or not during the GW data inference (and for which quantities), the templates might be used in fully informed, partially informed or agnostic approach. Importantly, *all* approaches require the quasiuniversal relations to extract astrophysical constraints, either *a priori* or *a posteriori*.

Most of the PM templates are built from a simple ansatz made of few damped sinusoids in the time domain, eventually represented in the frequency domain. Notable exceptions to a sinusoids basis are the models proposed in Refs. [37,39] where reduced basis were constructed directly from NR data. Reference [37] used a principal component analysis and ~50 nonspinning simulations (12 of which unequal masses) to demonstrate faithfulnesses $\gtrsim 0.9$ on a subsample of the data. Reference [39] used a hierarchical model trained on 35 nonspinning, equal-mass NR simulations to demonstrate fitting factors up to 0.98 on the training set. However, similar fitting factors can be achieved with significantly less modeling efforts in agnostic approaches based on wavelets or sinusoids basis [38,41,42,44]. Moreover, the finite precision of NR simulations introduces uncertainties that impact the faithfulnesses at ~0.9 level [11,39]. Hence, simpler analytical templates appear favored over more complex statistical models. The agnostic approach utilized in Refs. [38,44] delivers, on average, larger fitting factors to numerical data when compared to fully or partially informed approaches, e.g. [11,41–43]. This suggests that agnostic approaches are able to detect PM signals at a lower signal-to-noise ratio (SNR) because informed models are not sufficiently accurate. The two approaches, however, appear comparable at SNR relevant for astrophysical parameter estimation, and they deliver comparable constraints on the EOS. We stress that faithfulnesses calculations are often presented on validation datasets of different sizes and a detailed comparison is difficult. For example, [42] found faithfulnesses between 0.91–0.97 on a sample of nine simulations; [41] found faithfulnesses between 0.4–0.95 on a sample of 60 simulations, and [11] between 0.4–0.95 on a sample of about 150 simulations. A main motivation for (partially) informed approaches is the possibility to design inspiral-merger-postmerger templates by consistently extending inspiral-merger templates. In Ref. [11], we developed the first model of this kind by completing the EOB framework of Refs. [6,7] with the `NRPM` PM model.

The new `NRPMw` is a PM frequency-domain template that aims at striking a balance between fully informed and agnostic approaches. It is constructed by superposing few Gaussian, frequency-modulated wavelets whose parameters are informed by new EOS-insensitive relations. The latter build on the largest public databases of NR simulations available to date. The theoretical uncertainties of the EOS-insensitive relations are incorporated in the model using recalibration parameters that are determined during the inference. Hence, `NRPMw` performs best in a partially informed inference. The recalibration enhances the flexibility of the template and improves the fitting factors to a level similar to agnostic templates. Data analysis applications of `NRPMw` are presented in paper II.

The rest of this paper is structured as follows. In Sec. II, we discuss the PM waveforms' phenomenology predicted by state-of-art NR simulations. The modeling choices used in `NRPMw` are presented in Sec. III. The quasiuniversal relations calibrated for `NRPMw` are discussed in Sec. IV. In Sec. V we validate the model against NR data by calculating its faithfulness on an independent validation set. We summarize our findings and conclude in Sec. VI. Moreover, we include several Appendices in order to extend the discussions on the waveform modeling and on the calibration of EOS-insensitive relations.

Conventions. We use geometric units $c = G = 1$ or explicitly state units. Masses are expressed in solar masses $M_\odot$. The GW polarizations h_+ and $h_\times$, plus and cross, respectively, are decomposed in (ℓ, m) multipoles as

$$h_+ - \mathrm{i}h_\times = D_L^{-1} \sum_{\ell=2}^{\infty} \sum_{m=-\ell}^{\ell} h_{\ell m}(t)\,{}_{-2}Y_{\ell m}(\iota, \varphi), \quad (1)$$

where D_L is the luminosity distance, ${}_{-2}Y_{\ell m}$ are the $s = -2$ spin-weighted spherical harmonics and ι, φ are, respectively, the polar and azimuthal angles that define the orientation of the binary with respect to the observer. Each mode $h_{\ell m}(t)$ is decomposed in amplitude $A_{\ell m}(t)$ and phase $\phi_{\ell m}(t)$, as

$$h_{\ell m}(t) = A_{\ell m}(t)\mathrm{e}^{-\mathrm{i}\phi_{\ell m}(t)}, \quad (2)$$

with a related GW frequency,

$$\omega_{\ell m}(t) = 2\pi f_{\ell m}(t) = \frac{\mathrm{d}}{\mathrm{d}t}\phi_{\ell m}(t). \quad (3)$$

The moment of merger is defined as the time of the peak of $A_{22}(t)$, and referred simply as merger when it cannot be confused with the coalescence/merger process. If the multipolar indices (ℓ, m) are omitted from a multipolar quantity, we implicitly refer to the dominant (2, 2) mode. Note that the time t refers to the retarded time in the case of NR data. We define the Fourier transform $h_{\ell m}(f)$ of each multipolar mode as

$$h_{\ell m}(f) = \int_{-\infty}^{+\infty} h_{\ell m}(t)\mathrm{e}^{-2\pi \mathrm{i} f t}\mathrm{d}t. \quad (4)$$

Analogously to the time-domain case, the frequency series $h_{\ell m}(f)$ is decomposed in amplitude $A_{\ell m}(f)$ and phase $\phi_{\ell m}(f)$.

The binary mass is $M = m_1 + m_2$, where $m_{1,2}$ are the masses of the two stars, the mass ratio $q = m_1/m_2 \geq 1$, and the symmetric mass ratio $\nu = m_1 m_2/M^2$. We define the parameter $X = 1$–4ν. The dimensionless spin vectors are denoted with $\boldsymbol{\chi}_i$ for $i = 1$, 2 and the spin component aligned with the orbital angular momentum $\mathbf{L}$ are labeled as $\chi_i = \boldsymbol{\chi}_i \cdot \mathbf{L}/|\mathbf{L}|$. The effective spin parameter $\chi_{\rm eff}$ is the mass-weighted aligned spin, i.e.

$$\chi_{\rm eff} = \frac{m_1\chi_1 + m_2\chi_2}{M}. \tag{5}$$

Moreover, the quadrupolar tidal polarizability parameters are defined as $\Lambda_i = (2/3)k_{2,i}C_i^{-5}$ for $i = 1, 2$, where $k_{2,i}$ and C_i are, respectively, the $\ell = 2$ gravitoelectric Love number and the compactness of the ith NS. The tidal coupling constant is [46]

$$\kappa_2^{\rm T} = 3\nu\left[\left(\frac{m_1}{M}\right)^3\Lambda_1 + (1 \leftrightarrow 2)\right], \tag{6}$$

that, similarly to the reduced tidal deformability $\tilde{\Lambda}$ [47], parametrizes the leading-order tidal contribution to the binary interaction potential.

II. WAVEFORM MORPHOLOGY

The PM waveform morphology and its connection to the remnant's dynamics predicted by simulations was discussed in various papers, see e.g. Refs. [10,21,23,24,48–57]. We review here the main aspects that are relevant for the GW model proposed in the rest of the paper. Figure 1 shows the PM signal in exemplary cases; the time axis is shifted to the moment of merger.

A merger remnant is a massive, hot and rotating NS whose mass is usually larger than the maximum mass sustained by a cold, isolated Tolmann-Oppenheimer-Volkoff (TOV) NS. It can either collapse to a BH or settle to a stable rotating NS on secular timescales. Gravitational collapse to BH takes place as the remnant reaches densities comparable to the TOV's maximum density [58] since the remnant's core is very slowly rotating [59]. The remnant of a very massive BNS can promptly collapse after the moment of merger and crucially before the first bounce of the two cores [60,61].[1]

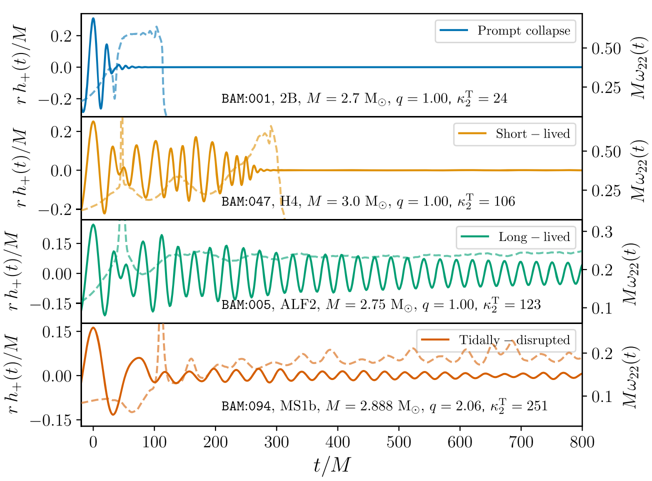

FIG. 1. Representative examples of BNS PM waveforms. The plot shows the plus polarization $h_+(t)$ of the time-domain $\ell = m = 2$ waveform (solid line) and the instantaneous GW frequency $\omega_{22}(t)$ (dashed line). The NR simulations are from the CORE database and computed in Refs. [6,48].

In the case of an equal mass BNS, the prompt collapse is described by empirical relations relating the binary mass to the TOV maximum mass and compactness proposed in Refs. [63,64] and refined in various works, e.g. [14,15]. For very asymmetric BNS, the tidal disruption of the secondary drives the gravitational collapse [57] and it is mainly controlled by the incompressibility parameter of nuclear matter around the TOV maximum density [58]. While a robust prompt collapse criterion is not known in these conditions [57,58,65], tidal disruption effects are of the order of current EOS effects in the equal-mass criterion, at least for mass ratio $q \lesssim 1.4$ [15,58]. Prompt collapse mergers have the largest GW luminosities (at merger) [24] but the PM signal is the rapidly damped ringdown of the BH and it is practically negligible for the sensitivities of current and next-generation detectors. A prompt collapse signal is showed in the top panel of Fig. 1.

The evolution of a NS remnant is driven by an intense emission of GWs lasting ∼10–20 milliseconds (GW-driven phase) [24,66]. During this phase, the remnant either collapses to BH (*short-lived* remnant) or settles to an approximately axisymmetric rotating NS (*long-lived* remnant).[2] The GW-driven phase is associated to a luminous GW transient at frequencies ∼2–4 kHz [10,21,49–51,53]. The spectrum of this transient is rather complex but has robust and well-studied features at a few characteristic frequencies. Most of the power is emitted in the $\ell = m = 2$ GW mode at a nearly constant frequency $\omega_{22}(t) \approx 2\pi f_2$. Examples of $\ell = m = 2$ waveforms for short- and long-lived remnants are shown in the three bottom panels of Fig. 1. The f_2 frequency is easily extracted from simulation data and it was shown to correlate with various binary quantities in a EOS-insensitive way, e.g. [10,11,23,53].

We stress that the PM spectrum is not composed of a discrete set of frequencies: the presence of broad peaks with typical full width at half maximum of 300–600 Hz is simply a consequence of the efficiency of the emission process. Indeed, inspection of the time-domain waveform's instantaneous frequency (see Fig. 1) shows that $\omega_{22}(t)$

[1] This definition of prompt collapse implies negligible shocked dynamical ejecta because the bulk of this mass ejection comes precisely from the first core bounce [62]. Since it directly connects to the main dynamical feature of the merger process (shock and bounce) and to related observables, it is preferable to other empirical definitions based on collapse time from the moment of merger.

[2] A commonly used terminology for short-lived remnant is hypermassive NS. This name is not appropriate for remnants since it refers to cold equilibrium. See [61,67] and references therein.

increases as the remnant becomes more compact and has a steep acceleration towards gravitational collapse,[3] see e.g. Fig. 1 of [10]. Moreover, the instantaneous GW frequency has modulations with frequencies $f_0 \sim O(1\ \mathrm{kHz})$ that are stronger for remnants closer to collapse. These modulations are associated to the violent radial bounces of the remnant's core prior to collapse. Other robust features of the spectrum are two secondary peaks at frequencies $f_{2\pm 0}$, respectively, at larger and smaller frequencies than f_2. These features are associated to hydrodynamical modes in the remnant, e.g. [50,68,69] and have been tentatively interpreted as non-linear coupling between f_2 and f_0 [50], in analogy to perturbations of rotating NS [70–72].

The remnant's signal from asymmetric binaries with mass ratio $q \gtrsim 1.5$ carries the imprint of the tidal disruption during merger [48,57]. An example is shown in the bottom panel of Fig. 1. The tidal disruption of the secondary object redistributes the matter over a larger volume surrounding the remnant. As a consequence, radial fluctuations are generally milder and the PM GW luminosity is smaller than the comparable-mass case. These dynamical features are reflected in the GW waveform. The PM amplitude can be significantly smaller than in the equal-mass cases and the peaks at frequencies $f_{2\pm 0}$ are typically suppressed. Moreover, for $q \gtrsim 1.5$, internal shocks and fluid flows can introduce multiple discontinuities in the time-domain GW phase.

The evolution of a NS remnant beyond the GW-driven phase is highly uncertain at present. It requires detailed simulations of viscous and nuclear processes on time-scales beyond hundreds of milliseconds, for example to quantify precisely the mass accreting or outflowing the central object. NS remnants after the GW-driven phase have an excess of both gravitational mass and angular momentum when compared to equilibrium configuration with the corresponding baryon mass [67,73]. Possible mechanisms to shed (part of) this energy are long-term GW instabilities [74,75] including one-arm instabilities [54,76], that would lead to potentially detectable, long GW transients at $\lesssim 1$ kHz.

The PM model presented in the next sections describes the GW transient during the GW-driven phase and it builds on our previous work in Refs. [10,11]. In particular, we devise new EOS-insensitive relations based on the tidal coupling constant κ_2^{T} and incorporate them in a partially informed model. We do not use empirical relations for modeling prompt collapse and instead design a model capable of inferring a generic collapse time from the observational data (but see e.g. Ref. [14] for an application of prompt collapse quasiuniversal relations in data analysis context). Similarly, we account for the theoretical uncertainties of the EOS insensitive using recalibration parameters inferred from the data.

III. NRPMw DESIGN

In order to develop an analytical NR-informed PM model for BNS mergers in the frequency domain, we first introduce a truncated complex Gaussian wavelet $W(t)$,

$$W(t;\alpha,\beta,\gamma,\tau) = \begin{cases} \mathrm{e}^{\alpha t^2+\beta t+\gamma} & \text{if } t\in[0,\tau] \\ 0 & \text{otherwise} \end{cases}, \tag{7}$$

where $\alpha,\beta,\gamma \in \mathbb{C}$ are time-independent parameters and the real interval $[0,\tau]$ defines the nonvanishing support of W. The coefficients $\{\alpha,\beta,\gamma\}$ can be interpreted as follows: $\Re(\alpha)$ and $\Re(\beta)$ determine, respectively, the concavity and the initial slope of the time-domain wavelet amplitude; $\Im(\alpha)$ and $\Im(\beta)$ define, respectively, the slope and the initial value of the time-domain frequency evolution; γ is an overall factor determining initial amplitude and phase.

The frequency-domain wavelet $W(f)$ can be analytically computed from Eq. (7) using Gaussian integrals,

$$W(f) = \frac{\mathrm{e}^{\gamma}}{2}\sqrt{\frac{\pi}{\alpha}}\mathrm{e}^{-z^2}[\mathrm{erfi}(z+\sqrt{\alpha}\tau) - \mathrm{erfi}(z)], \tag{8}$$

where $z(f)$ encodes the frequency dependency,

$$z(f) = \frac{\beta - 2\pi \mathrm{i} f}{2\sqrt{\alpha}}, \tag{9}$$

and $\mathrm{erfi}(z)$ is the imaginary error function. For $\alpha = 0$, Eq. (8) is not defined and it is directly replaced by a Lorentzian function. Moreover, a direct implementation of Eq. (8) can lead to floating point overflow fin a certain portion of the parameter space. In these cases, we employ the analytical approximations discussed in Appendix A. Furthermore, we introduce a global time shift τ_0 in order to allow the wavelet to move on the time axis. The time shift τ_0 changes the wavelet support to $[\tau_0, \tau+\tau_0]$ and it is easily implemented by a unitary factor, i.e. $W(f;\tau_0) = W(f)\mathrm{e}^{-2\pi \mathrm{i} f \tau_0}$.

The wavelet is the basic component of NRPMw. In the following paragraphs we describe how different wavelets are combined based on the universal features of the PM signal that are identified by characteristic times ("nodes," Sec. III A). Then, we discuss the modeling of subdominant frequencies as additional wavelet modulations in Sec. III B. The basic construction of the dominant $\ell = m = 2$ mode is discussed Sec. III C and the modeling of higher-order modes in Sec. III D.

A. Nodal points

The time-domain strain has universal characteristic features at specific times, as pointed out in Ref. [11]

[3]Considering gauge-invariant energetics it is possible to associate to the remnant a dynamical frequency Ω such that $f_2 = \Omega/\pi$ and analogously for other modes.

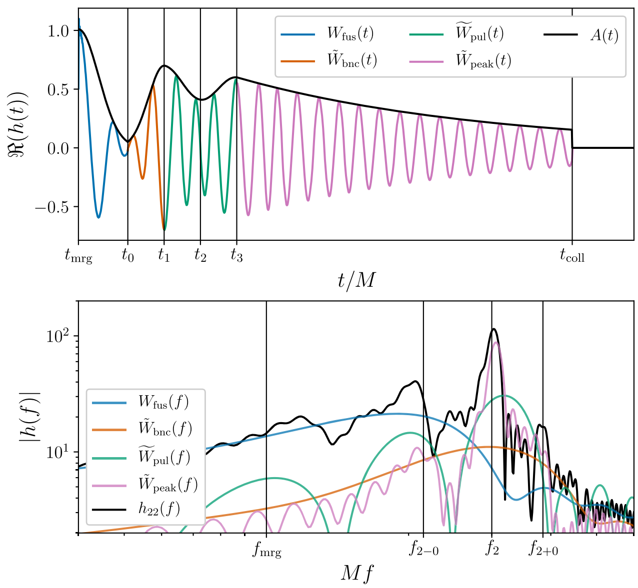

FIG. 2. Exemplary case showing the morphology of NRPMw model. Different wavelet components are reported with different colors: $W_{\rm fus}$ in blue, $\tilde{W}_{\rm bnc}$ in orange, $\tilde{W}_{\rm pul}$ in green, and $\tilde{W}_{\rm peak}$ in purple. The top panel shows the time-domain components and the overall GW amplitude $A(t)$ (black line) highlighting the characteristic times with vertical lines, i.e. the time of the merger $t_{\rm mrg}$, the nodal points t_i for $i = 0, 1, 2, 3$ and the time of collapse $t_{\rm coll}$. The bottom panel shows the Fourier spectra of each component, the overall h_{22} spectrum (black line) and the characteristic PM frequencies (vertical lines), i.e. the merger frequency $f_{\rm mrg}$, the PM peak f_2 and the subdominant couplings $f_{2\pm 0} = f_2 \pm f_0$.

(see also Fig. 2). We call these times *nodal points* and indicate them as $\{t_i\}$ for $i = 0, 1, 2, 3$. Nodal points are identified as stationary points of the strain's amplitude, that we indicate as $\{A_i\}$. As discussed in Ref. [11], NR simulations show that in correspondence of the amplitude minimum ($t = t_0$), the time-domain GW frequency $\omega_{22} = -\Im(\dot{h}_{22}/h_{22})$ is singular and the phase has a discontinuity (see also Refs. [77–79].) Differently from Ref. [11], we assume $t_{i+1} - t_i$ to be constant, for $i = 0, 1, 2$. Hence, the nodal points can be reduced to two independent parameters: the moment t_0 of the first amplitude's minimum after merger, and a characteristic timescale T_0 that is computed as the difference $t_3 - t_1$. The timescale T_0 defines the subdominant frequency $f_0 \simeq {T_0}^{-1}$ that characterizes the modulations of the PM signal. Note that the subdominant component f_0 has in general a non-negligible time dependency, as shown by NR simulations (e.g. [79,80]). A further time-domain node is introduced for the time of the remnant collapse $t_{\rm coll}$. Differently from [11], here we do not introduce t_4.

B. Amplitude and frequency modulations

Ampitude and frequency modulations (AMs, FMs) are prominent features of the PM spectrum, as discussed in Sec. II. NR simulations show that the main GW modulations are given in the $m = 0$ channel, and are associated to the quasiradial density oscillations of the remnant [81]. We associate this mode to the fundamental frequency f_0 and, for the modeling of the (2, 2) mode, we consider only the modulation couplings between f_2 and f_0.[4] Moreover, we neglect possible frequency evolution of the subdominant mode f_0, i.e. this frequency component is assumed to be constant in time. Modulation effects appear after the collision of the NS cores, for $t > t_0$, when the remnant is strongly deformed and dynamically unstable.

AMs can be easily taken into account by employing a combination of wavelets. Labeling the amplitude-modulated wavelet as $\breve{W}$, we can write

$$\begin{aligned}\breve{W}(t) &= W(t)[1 + \Delta_{\rm am} \sin(\Omega_{\rm am} t + \phi_{\rm am})],\\ &= W(t) - \frac{{\rm i}\Delta_{\rm am}}{2} \sum_{k=\pm 1} k W(t) {\rm e}^{{\rm i}k(\Omega_{\rm am} t + \phi_{\rm am})},\end{aligned} \tag{10}$$

where $\Delta_{\rm am}$ defines the magnitude, $\Omega_{\rm am}$ the modulation frequency and $\phi_{\rm am}$ the initial phase of the AMs. Equation (10) can be transformed in the Fourier space obtaining

$$\breve{W}(f) = W(f) - \frac{{\rm i}\Delta_{\rm am}}{2} \sum_{k=\pm 1} k W^{(k)}(f), \tag{11}$$

where

$$W^{(k)}(f) = W(f; \alpha, \beta + {\rm i}k\Omega_{\rm am}, \gamma + {\rm i}k\phi_{\rm am}, \tau). \tag{12}$$

Equation (11) shows explicitly that an amplitude-modulated wavelet $\breve{W}$ can be easily written in terms of the Gaussian wavelets W and it introduces two subdominant contributions in the Fourier domain that are displaced with respect to the primary peak of $\pm\Omega_{\rm am}$.

FMs affect the phase evolution of the time-domain wavelet. We implement a FM wavelet $\tilde{W}$ defining the frequency evolution as

$$\omega_{\tilde{W}}(t) = \omega_W(t) - \Delta_{\rm fm} {\rm e}^{-\Gamma_{\rm fm} t} \sin(\Omega_{\rm fm} t + \phi_{\rm fm}), \tag{13}$$

where $\omega_{\tilde{W}}$ is the instantaneous frequency of the frequency-modulated wavelet $\tilde{W}$, ω_W is the instantaneous frequency of the Gaussian wavelet W, and $\Delta_{\rm fm}, \Gamma_{\rm fm}, \Omega_{\rm fm}, \phi_{\rm fm} \in \mathbb{R}$ are the parameters that define the FM, i.e. $\Delta_{\rm fm}$ is the initial frequency displacement, $\Gamma_{\rm fm}$ the inverse damping time, $\Omega_{\rm fm}$ the modulation frequency and $\phi_{\rm fm}$ the initial phase. Using Taylor expansion, the frequency-modulated wavelet $\tilde{W}$ can be rewritten in terms of the frequency-domain Gaussian wavelet W. A detailed discussion on the analytic form of

[4]Our simulations indicate that the couplings between (2, 1) and (3, 3) modes can also be relevant for unequal-mass BNS.

$\tilde{W}(f)$ is provided in Appendix B. Note that, differently from the AMs shown in Eq. (10), the FM contribution presented in Eq. (13) includes damped behavior, i.e. $\Gamma_{\rm fm} \neq 0$ *a priori*. This term is needed to properly characterize the different timescales of the PM frequency components f_2 and f_0.

Combining the definitions of $\breve{W}$, Eq. (11), and $\tilde{W}$ [see Eq. (B8)], it is possible to write a general modulated Gaussian wavelet, labeled as $\tilde{W}$. We consider AMs over the interval $[t_0, t_3]$ and FM for $t > t_0$. We fix the modulation frequencies to $\Omega_{\rm am} = \Omega_{\rm fm} = 2\pi f_0$. Then, the AM magnitude $\Delta_{\rm am}$ and phase $\phi_{\rm am}$ are fixed by the values of the GW amplitudes at the nodal points nodal points, i.e. $\{t_i, A_i\}$ for $i = 1, 2, 3$. The FM inverse damping time $\Gamma_{\rm fm}$ is assumed to be identically zero for $t < t_1$; then, it is fixed to a constant positive value calibrated on NR data (see Sec. IV). Furthermore, NR simulations show that AMs and FMs approximately fluctuate in opposite directions [11]; i.e. amplitude maxima occur at frequency minima and vice versa. The FM phase $\phi_{\rm fm}$ is fixed in order to satisfy this requirement.

C. Wavelet combination

The NRPMw model is constructed by describing each part of the PM signal between different nodal points with a modulated wavelet component. The overall strain h_{22} is computed summing all the contributions. The use of wavelets allow us to assign a clear interpretation of each parameter employed in the model. The combination of different wavelets can capture rather complex signal morphologies.

In NRPMw, the physical quantities (times, amplitudes and frequencies) are estimated using quasiuniversal relations calibrated on NR simulations (see Sec. IV). This allows us to design a fully informed model that can connect the signal's morphology to the intrinsic parameters of the BNS system (masses, spins and tidal parameters). However, some wavelet parameters could be left unconstrained and directly inferred from observational data [42] or they could be reconstructed with regression methods directly from NR simulations [39].

The time-domain $\ell = m = 2$ mode is modeled employing a combination of four different wavelet components,

$$h(t) \approx W_{\rm fus}(t) + \tilde{W}_{\rm bnc}(t) + \tilde{W}_{\rm pul}(t) + \tilde{W}_{\rm peak}(t), \qquad (14)$$

assuming continuity in amplitude and phase (except for a phase-shift $\phi_{\rm PM}$, see later) for the time-domain counterpart. Detailed expressions are given in Appendix C. The combination of wavelets includes the following terms that are shown in color in Fig. 2:

(1) $W_{\rm fus}$ describes the signal after merger and up to t_0, corresponding to the fusion of the NS cores. The wavelet has an initial frequency $f_{\rm mrg}$ and nonvanishing frequency drift that can be positive or negative depending on the properties of the binary.

(2) $\tilde{W}_{\rm bnc}$ describes the signal corresponding to the bounce after the collision of the cores. The phase here has a discontinuity $\phi_{\rm PM}$ at t_0. Moreover, for $t > t_0$, all wavelets include FMs with the subdominant frequency f_0.

(3) $\tilde{W}_{\rm pul}$ describes the emission up to t_3 during which the remnant is typically highly dynamical. Since the largest amount of the GW luminosity is emitted at times $\lesssim 5$ ms [24], this component also includes AMs with the subdominant frequency f_0.

(4) $\tilde{W}_{\rm peak}$ describes the signal after the luminosity peak by a damped sinusoidal with initial frequency f_2, a frequency evolution parametrized by the drift $\alpha_{\rm peak}$ [also referred as $\Im(\alpha_{\rm peak})$ in Appendix C]. This component characterizes the dominant Fourier peak and it lasts until the time of collapse $t_{\rm coll}$.

Additionally, the GWs emitted by the collapse and BH ringdown can be modeled as a fifth term in Eq. (14), $W_{\rm coll}$ (see Appendix C for a detailed discussion). Knowing the properties of the final BH, this component could be modeled with the quasinormal modes of the remnant [82,83]. For simplicity, however, we set here $W_{\rm coll} = 0$.

Figure 2 shows an example of the discussed contributions in time and frequency domain, with the different terms appearing in Eq. (14) shown in different colors. The overall spectrum shows the typical PM patterns: the dominant PM peak associated to f_2, a weaker peak at lower frequencies corresponding to the merger dynamics and subdominant peaks due to AMs and FMs. The superposition of the wavelet components generates several local minima and maxima in the overall h_{22} spectrum. Moreover, the destructive interference of the wavelets originates a local minimum typically located between $f_{\rm mrg}$ and f_2. This feature is also generally observed in BNS PM spectra extracted from NR simulations. Moreover, the sharp cut at $t_{\rm coll}$ in time-domain waveform originates the ringing effects observed in the h_{22} spectrum.[5] The further inclusion of $W_{\rm coll}$ will mitigate this effect, yielding to a smoother waveform representation.

Overall, the model is characterized by 17 parameters, that are the characteristic frequencies, amplitudes, times and phases that define instantaneous GW amplitude and frequency (see Appendix C). Most of these quantities can be related to the binary properties using NR information.

D. Higher-order modes

NR simulations show prominent coupling effects in higher mode (HM) terms of BNS PM transients, similarly to what we discussed for the dominant (2, 2) mode. Also for this reason, the power of HM contributions in BNS PM

[5]This can be easily seen performing the convolution product of a sinusoidal wavelet with a Heaviside function.

radiation is considerably larger compared with the premerger dynamics [57,84]. For typical BNS systems, these contributions cover a relatively broad spectrum, roughly from ~500 Hz to 5–7 kHz.

In general, HM contributions can be modeled as a combination of wavelets with different frequencies imposing continuity in amplitude and phase. For $m \neq 0$, the characteristic peak frequencies of HMs can be approximated using the quadrupolar term employing the multipolar scaling, i.e. $f_{\ell m} \simeq (m/2) f_2$. However, the hierarchy of frequency couplings is not fully resolved. A detailed analysis of these subdominant features might require better resolved simulations to robustly identify the trend in the spectra. We remand the inclusion of HM PM characteristic properties to a future study.

IV. NR CALIBRATION

The NRPMw model has 17 parameters, i.e.

$$\begin{aligned}\boldsymbol{\theta}_{\rm PM} = \{&\phi_{\rm PM}, \phi_{\rm fm}, t_0, t_{\rm coll},\\ &A_{\rm mrg}, A_0, A_1, A_2, A_3,\\ &f_{\rm mrg}, f_2, f_0, \Delta_{\rm fm}, \Gamma_{\rm fm},\\ &\Re(\beta_{\rm peak}), \Im(\alpha_{\rm fus}), \alpha_{\rm peak}\},\end{aligned} \tag{15}$$

that can be mapped to the binary parameters,

$$\boldsymbol{\theta}_{\rm bin} = \{m_1, m_2, \Lambda_1, \Lambda_2, \chi_1, \chi_2\}, \tag{16}$$

using NR simulations. We chose to map only a subset of $\boldsymbol{\theta}_{\rm PM}$ and let some other parameters to be determined by the inference or any other minimization procedure with given data. In particular, we map the following 13 parameters:

$$\begin{aligned}\boldsymbol{\theta}_{\rm fit} = \{&A_{\rm mrg}, A_0, A_1, A_2, A_3, f_{\rm mrg}, f_2, f_0, t_0,\\ &\Re(\beta_{\rm peak}), \Im(\alpha_{\rm fus}), \Delta_{\rm fm}, \Gamma_{\rm fm}\}'.\end{aligned} \tag{17}$$

We fix $\phi_{\rm fm}$ by the AMs and the FMs as discussed in Sec. III B, and we leave three additional degrees of freedom,

$$\boldsymbol{\theta}_{\rm free} = \{\phi_{\rm PM}, t_{\rm coll}, \alpha_{\rm peak}\}. \tag{18}$$

This choice is motivated by the fact that these three parameters cannot be robustly mapped using NR data. The PM phase $\phi_{\rm PM}$ shows a strong dependence on the simulation's grid resolutions and on the physical models, e.g. [77,85,86]. The time of collapse $t_{\rm coll}$ is difficult to robustly determine from simulations due its dependence on grid resolution [11]; moreover, it strongly depends on the properties of the nuclear EOS and might be biased by the relatively small EOS set available [16,25,87]. The frequency drift $\alpha_{\rm peak}$ is also connected to the collapse dynamics and, as such, it can be affected by various processes, especially in long-lived remnants. For example, we discuss in Appendix D the dependency of $\alpha_{\rm peak}$ on the turbulent viscosity in a subset of simulations.

The calibration set of binaries includes the public available nonprecessing NR simulations of the CORE [88,89] and the SACRA [90–92] databases, plus additional data from simulations of Refs. [16,57,93] with the BLh and BLQ EOS. The CORE database includes data computed with two different NR codes, BAM [94,95] and THC [96] and simulate microphysics, neutrino transport (with various schemes) and turbulent viscosity. The final dataset is composed by 618 simulations and it includes 190 different binary configurations computed with three independent NR codes and 21 different EOSs. The finite temperature, composition-dependent EOSs are BHB$\Lambda\phi$ [97], BLh [98,99], BLQ [16,98,99], HS(DD2) [[100,101] DD2 hereafter], LS220 [102], SFHo [103], SRO(SLy) [[104] SLy hereafter]; the EOSs in piecewise polytropic forms are these: ALF2 [105], ENG [106], MPA [107], MS1 [108], MS1b [108], SLy [109], 2B, 2H, 15H, 125H, B, H, H4, HB from Refs. [110,111] and the $\Gamma = 2$ ideal gas EOS. We remark that ALF2 and BLQ include a phase transition to deconfined quark matter, and BHB$\Lambda\phi$ takes into account the appearance of hyperons at high densities. The intrinsic parameters of the data cover the ranges $M \in [2.4, 3.4] M_\odot$, $q \in [1, 2]$, $\kappa_2^{\rm T} \in [22, 458]$ and $\chi_{\rm eff} \in [-0.14, +0.22]$. Among the considered dataset, 80 simulations (~13% of the sample) resulted in prompt collapse and ~40% of the total data is composed by equal-mass nonspinning binaries. We include all available resolutions for every binary configuration and we treat each point as an independent measure in order to improve the characterization of NR uncertainties. The quasiuniversal relations presented in this work extend those in Ref. [11] including effects of large mass ratios, i.e. $q > 1.5$, and aligned spins with $|\chi_{\rm eff}| \lesssim 0.2$. In Appendix F, we present a recalibration of the quasiuniversal relations between the PM peak frequency f_2 and the NS radius that is not used in NRPMw but often employed in GW inference.

The mapping between binary and NRPMw parameters is performed on the *mass-rescaled* PM parameters using a factorized fitting function (for any quantity Q),

$$Q^{\rm fit} = a_0 Q^{\rm M}(X) Q^{\rm S}(\hat{S}, X) Q^{\rm T}(\kappa_2^{\rm T}, X), \tag{19}$$

where $Q^{\rm M} = 1 + a_1^{\rm M} X$ includes the mass ratio contributions in terms of the $X = 1–4\nu$ parameter; $Q^{\rm S} = 1 + p_1^{\rm S} \hat{S}$ takes into account spin corrections in terms of the spin parameter [112]

$$\hat{S} = \left(\frac{m_1}{M}\right)^2 \chi_1 + \left(\frac{m_2}{M}\right)^2 \chi_2, \tag{20}$$

and $p_1^{\rm S} = a_1^{\rm S}(1 + b_1^{\rm S} X)$. The term

TABLE I. Summary of the quasiuniversal relations for the PM parameters $\boldsymbol{\theta}_{\rm fit}$ as functions of the inspiral parameters $\boldsymbol{\theta}_{\rm bin}$. The first column report the quantity of interest and the second column shows the range spanned by the available NR data. From the third to the 14th column, we report the calibrated coefficients of the quasiuniversal relations. The last three columns show, respectively, the χ^2, the relative standard deviation of the fit and the Kullback-Leibler divergence $D_{\rm KL}$ between the recovered residuals and a normal distribution.

$Q^{\rm fit}$	Range	a_0	$a_1^{\rm M}$	$a_1^{\rm S}$	$b_1^{\rm S}$	$a_1^{\rm T}$	$a_2^{\rm T}$	$a_3^{\rm T}$	$a_4^{\rm T}$	$b_1^{\rm T}$	$b_2^{\rm T}$	$b_3^{\rm T}$	$b_4^{\rm T}$	χ^2	Error	$D_{\rm KL}$
$A_{\rm mrg}/M$	[0.159, 0.313]	0.3948	−1.133	−0.02992	−2.593	0.03902	5.1846×10^{-5}	0.06033	1.380×10^{-4}	10.41	54.51	10.83	54.54	0.189	1.8%	0.26
A_0/M	[2.04×10^{-4}, 0.0699]	0.02356	0	1.077	260.4	-1.318×10^{-3}	0	0	0	−4.314	0	0	0	267	66%	0.14
A_1/M	[0.0262, 0.238]	−0.05641	−5	−1.135	146.8	−0.8343	3.882×10^{-4}	0.2464	0	−5	0	0	0	13.2	15%	0.18
A_2/M	[4.76×10^{-4}, 0.175]	0.1667	−5.135	−3.796	−28.47	0	0	5.774×10^{-3}	0	0	0	4.027×10^{-8}	0	78.2	38%	0.077
A_3/M	[5×10^{-3}, 2.04×10^{-1}]	0.1662	0.1072	−2.046	−45.06	-7.06×10^{-5}	0	1.354×10^{-3}	0	−1423	0	284.7	0	38.4	26%	0.044
$Mf_{\rm mrg}/\nu$	[0.0554, 0.141]	0.2276	0.9233	0.5938	−1.994	0.03445	5.58×10^{-6}	0.08405	1.133×10^{-4}	13.83	517.4	12.75	139.8	0.431	2.6%	0.45
Mf_2	[0.0216, 0.0512]	0.0881	22.81	0.2925	25.0	0.007023	-1.782×10^{-6}	0.02587	6.58×10^{-6}	5.428	0	39.29	0	0.814	3.9%	0.029
Mf_0	[1.86×10^{-3}, 0.0441]	0.02734	19.32	−1.857	−75.77	-2.967×10^{-3}	8.484×10^{-6}	8.584×10^{-3}	0	20.49	21.5	10.47	0	107	45%	0.10
M/t_0	[8.09×10^{-3}, 0.0288]	0.03265	0.2994	−0.2329	4.768	3.584×10^{-3}	0	0.01053	0	−11.96	0	−3.22	0.0	5.11	9.2%	0.72
$M\Re(\beta_{\rm peak})$	[6×10^{-4}, 6.58×10^{-3}]	0.1912	4.074	−1.573	100	0.05884	0	3.896	0	−5.293	0	0	0	37.7	27%	0.042
$M^2\Im(\alpha_{\rm fus})/\nu$	[-3.3×10^{-4}, 5×10^{-3}]	0.003721	−1.799	0.3555	−7.167	0.0139	-2.425×10^{-5}	0.05883	1.882×10^{-4}	−28.64	−36.18	19.53	7.089	346	75%	3.7
$M\Delta_{\rm fm}$	[1.5×10^{-4}, 0.0423]	0.05139	0.4944	−3.734	−145	-6.25×10^{-3}	1.728×10^{-5}	0.01944	0	−7.936	1.882	100	0	278	74%	0.041
$M\Gamma_{\rm fm}$	[0, 0.05]	0.1637	209.3	−0.2997	24.5	0.02195	0	0.3528	0	−0.5111	0.	74.72	0	326	98%	1.05

$$Q^{\rm T}=\frac{1+p_1^{\rm T}\kappa_2^{\rm T}+p_2^{\rm T}\kappa_2^{\rm T2}}{1+p_3^{\rm T}\kappa_2^{\rm T}+p_4^{\rm T}\kappa_2^{\rm T2}}, \tag{21}$$

takes into account tidal effects in terms of $\kappa_2^{\rm T}$ and with $p_i^{\rm T}=a_i^{\rm T}(1+b_i^{\rm T}X)$. The coefficients $\{a_i^{\cdot},b_i^{\cdot}\}$ are determined fitting the NR data. We note that the choice of the fitting function in Eq. (19) might be neither unique nor optimal; we have experimented with few functions and found Eq. (19) sufficiently simple, general and accurate for our purposes. The choice of a rational function for $Q^{\rm T}(\kappa_2^{\rm T})$ is instead motivated by previous works [10,11,113,114]. Finally, we stress the importance of using mass-rescaled quantities in quasiuniversal relations [10,11]; Appendix F demonstrates that factorizing the (trivial) binary mass scale is key to obtain EOS-insensitive relations.

The fitting is performed using a least squared method. Denoting by $Q_i^{\rm NR}$ any NR quantity of interest extracted from the ith NR simulation and $Q_i^{\rm fit}$ its fit, we define the relative residual of the ith NR simulation,

$$r_i=\frac{Q_i^{\rm fit}-Q_i^{\rm NR}}{Q_i^{\rm fit}}, \tag{22}$$

and minimize $\chi^2=\sum_i r_i^2$. For each calibrated PM parameter, Table I reports the calibrated coefficients and the associated relative error, defined as the standard deviation of the relative residuals, i.e. $\sqrt{{\rm Var}(r_i)}$. For later purposes (see Sec. VA), we report in Table I the Kullback-Leibler divergence $D_{\rm KL}$ between the distribution of the residuals r_i and a normal distribution with zero mean and variance ${\rm Var}(r_i)$. This quantity allows us to verify the Gaussian character of the residuals.

In the following, we discuss the fit results, i.e. empirical relations for the merger properties (Sec. IVA), for the characteristic PM frequencies and amplitudes (respectively, Secs. IV B and IV C) and for the late-time properties (Sec. IV D).

A. Merger properties

Among all the quantities of interest, the amplitude and the frequency at merger, respectively, $A_{\rm mrg}$ and $f_{\rm mrg}$, are properties that can be extracted with good accuracy from NR data [11,113]. Our new relations have 1-σ errors smaller than 3%, as shown in Table I. These relations are constructed to match the binary black hole values for $\kappa_2^{\rm T}\to0$; the limiting values are taken from the EOB model of Ref. [112].

The slope parameter $\Im(\alpha_{\rm fus})$ characterizes the derivative of the GW frequency immediately after merger, i.e. $\Im(\alpha_{\rm fus})\propto({\rm d}f/{\rm d}t)_{\rm mrg}$. For every NR simulation, we estimate this property from the (2, 2) time-domain waveform as the mean value of ${\rm d}f/{\rm d}t$ taken in the range $[t_{\rm mrg},t_0]$. The calibrated relation for $\Im(\alpha_{\rm fus})$ shows larger uncertainties compared to $f_{\rm mrg}$, as reported in Table I. However, the presented relation shows clear trends in the tidal parameter and in the mass ratio. In particular, large-mass-ratio binaries (i.e. $q\gtrsim1.5$) show $\Im(\alpha_{\rm fus})\lesssim0$ due to tidal disruption.

Another early PM quantity is the time of the first amplitude minimum t_0. This quantity is extracted from the time-domain waveform and can be well captured by the our relations within ∼10%. NR simulations of binaries with $q\gtrsim1.5$ generally show increasing t_0 due to tidal disruption. Also the calibrated relations for $\Im(\alpha_{\rm fus})$ and t_0 include a robust binary black hole limit for $\kappa_2^{\rm T}\to0$ within the nominal error bars.

B. PM frequencies

We extract the main PM frequency f_2 from NR PM spectra of the (2, 2) mode. Generally, the f_2 frequency is estimated as the global maximum of the PM spectrum;

however, when modulations are prominent and the PM portions are short (i.e. $\lesssim 8$ ms), the f_2 contribution is no longer the dominant peak and it needs to be identified in the local maxima. As shown in Table I, the quasiuniversal relation for f_2 is accurate to $\sim 4\%$ at $1-\sigma$ level (6–7% at 90% credibility level), that corresponds to an error of about 100 Hz (200 Hz). The latter is typically smaller than the full width at half maximum of the spectrum peaks. Figure 3 shows this quasuniversal relation: the frequency Mf_2 primarily correlates with the tidal polarizability κ_2^{T}, while mass ratio and spin contributions mildly affect the overall value of this quantity.

The bottom panel of Fig. 3 shows data points with deviations larger than $2-\sigma$. Around $\kappa_2^{\mathrm{T}} \simeq 207$, it is possible to identify a cluster of NR data corresponding to spinning unequal-mass H4 binaries $1.65 + 1.10 M_\odot$ with different combinations of spins [48,56]. For these large mass-ratio cases, the spin correction employed in Eq. (19) will be improved in a future work when more data will be available. The largest residual ($\sim 15\%$) is given by the nonspinning equal-mass binaries BHB$\Lambda\phi$ $1.50 + 1.50 M_\odot$ [25] and BLQ $1.40 + 1.40 M_\odot$ [16]. In both cases, the remnant collapses into BH shortly after merger, i.e. $t_{\mathrm{coll}} \simeq 3$ ms, and the determination of the peak and secondary frequencies from this signal is rather delicate due to the short duration of the transient. From the Fourier spectra, it is possible to identify two dominant broad peaks at frequencies $Mf_{2\text{–}0} \simeq 0.036$ and $Mf_2 \simeq 0.048$ for the BHB$\Lambda\phi$ binary and $Mf_{2\text{–}0} \simeq 0.036$ and $Mf_2 \simeq 0.047$ for the BLQ binary. These values agree with the estimate of Mf_0 coming from the instantaneous GW frequency; however, the peak widths vary depending on the window used to smooth the NR data and it is not possible to clearly identify a carrier frequency and a modulation magnitude from the time-domain waveform.[6] Consistently with Ref. [11] we chose to identify the second peak with f_2 and conservatively include it in the determination of the quasiuniversal relation. In contrast, the choice of the first peak as f_2 would be consistent with Refs. [16,25], and the datapoints would not be outliers in the residual plot.

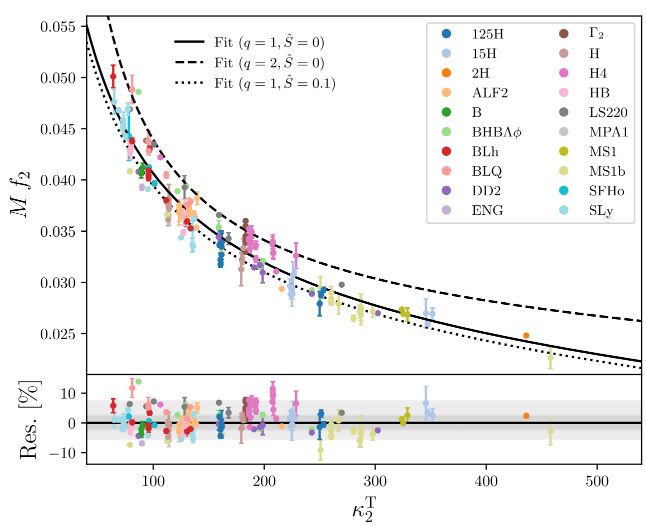

FIG. 3. Quasiuniversal relation for the PM peak frequency f_2 as function of the tidal polarizability κ_2^{T}. Top panel: calibrated relations (black lines) compared to NR data (colored dots) extracted from the CORE and the SACRA databases. Each color corresponds to a different EOS. NR medians and error bars are reported averaging over different numerical resolutions (when available) for the same binary configuration. Bottom panel: relative residuals between the calibrated relation and the NR data validation set. The gray areas show the 50% (dark) and 90% (light) credible regions of the residuals.

The value of the frequency f_0 is estimated as $f_0 = T_0^{-1} \simeq (t_3 - t_1)^{-1}$ (Sec. III A). The frequency f_0 shows a nonmonotonic dependency on the tidal coupling κ_2^{T} for $q \simeq 1$. For large mass ratio, i.e. $q > 1.5$, the NR-calibrated relation predicts a decreasing f_0 with typical values of $O(10^{-3})$. The relative error associated with f_0 is $\sim 60\%$, which is considerably larger than the error on the peak frequency f_2. This uncertainty can be related to the method used to estimate f_0 and to the numerical error that affects amplitude fluctuations. In principle, the frequency f_0 can be also extracted from the $(\ell = 2, m = 0)$ mode of the GW waveform. However, numerical errors appear to be larger for HM components, due to the lower magnitude of the strains, and the corresponding spectra do not show neat and unambiguous Fourier peaks, yielding to less accurate calibrated relations.

C. PM amplitudes

The PM amplitudes A_1, A_2 and A_3 are extracted from the time-domain NR data and they show a decreasing trend for increasing κ_2^{T} and for increasing mass ratio, similarly to Ref. [11]. This can be understood as the effects of stiffer EOSs and larger mass ratios that produce less violent dynamics in the remnant (for a fixed M). As a consequence of tidal disruption, the first amplitude A_0 increases with increasing mass ratio. Overall, these quantities show errors between 15% and 40%, except for A_0, which shows an error $\gtrsim 60\%$ since this quantity is comparable in magnitude to NR errors.

D. Late-time features

The damping time $\Re(\beta_{\mathrm{peak}})$ of the decaying tail in `NRPMw` is estimated from NR data using the approximation for exponential sinusoidal functions, i.e. $\Re(\beta_{\mathrm{peak}}) \simeq \max(A(t))/[2\max(A(f))]$, where $\max(A(t))$ is the maximum amplitude of the time-domain waveform and $\max(A(f))$ is the maximum amplitude of the frequency-domain spectrum. Despite errors of $\sim 30\%$, the calibrated relation has a

[6] We used a sinusoidal transition window centered around merger with different transition lengths in order to remove the inspiral contributions.

physically reasonable trend. For example, $\Re(\beta_{\rm peak})$ decreases for increasing mass ratios, in agreement with the tidally disruptive dynamics of high-mass ratio mergers.

The FM displacement $\Delta_{\rm fm}$ is estimated from the time-domain NR waveforms as the largest displacement in the instantaneous GW frequency $f_{22}(t)$ from the PM peak f_2. The $\Delta_{\rm fm}$ predictions show similar trends and comparable values to f_0 for equal-mass binaries. More significant differences emerge instead as the mass-ratio get larger. The FM damping time $\Gamma_{\rm fm}$ is also estimated from the time-domain NR data fitting a damped sinusoidal to the instantaneous GW frequency. This quantity has the less accurate relation among the presented cases (∼90%) due to the large errors introduced by the extraction method.

V. VALIDATION

We validate the NRPMw model by computing its faithfulness $\mathcal{F}$ against 102 NR waveforms of Refs. [11,57,62,73,93,115] that were not used for the calibration. Among the considered simulations, 12 binaries show prompt collapse into BH. The validation set is composed by NR simulations of nonspinning BNS performed with THC [96] that include different neutrino treatments, turbulent viscosity schemes and five EOSs, i.e. BHBΛϕ [97], DD2 [100], LS220 [102], SFHo [103] and SLy [109]. The intrinsic binary properties cover the ranges $M\in[2.6,3.4]M_\odot$, $q\in[1,1.8]$ and $\kappa_2^{\rm T}\in[47,199]$. The unfaithfulness $\bar{\mathcal{F}}=1-\mathcal{F}$ between two waveform templates, say h_1 and h_2, is defined as

$$\bar{\mathcal{F}}(h_1,h_2)=1-\max_{t_{\rm mrg},\phi_{\rm mrg}}\frac{(h_1|h_2)}{\sqrt{(h_1|h_1)(h_2|h_2)}},\qquad(23)$$

where the maximization is performed over the coalescence time and phase, respectively, $t_{\rm mrg}$ and $\phi_{\rm mrg}$. The inner product $(h_1|h_2)$ is

$$(h_1|h_2)=4\Re\int\frac{h_1^*(f)h_2(f)}{S_n(f)}\,\mathrm{d}f,\qquad(24)$$

where $S_n(f)$ is the power spectral density (PSD) of the detector. We employ the PSD curve of the next-generation detector ET [2,3] (configuration D). The unfaithfulness is computed between the PM part of the NR waveform and the NRPMw for the same intrinsic parameters, i.e. $\bar{\mathcal{F}}(h_{\rm NR},h_{\rm NRPMw})$, over the frequency range [1, 8] kHz.

Moreover, we compare the NR faithfulness of NRPMw to that of the time-domain NRPM model introduced in Ref. [11]. Note that NRPM can be also enhanced with the parameters $\{\alpha,\beta,\phi_{\rm PM}\}$ [17], that are analogous to $\{\alpha_{\rm peak},t_{\rm coll},\phi_{\rm PM}\}$ for NRPMw and further discussed in Appendix E. The main differences between the two models are the following. The frequency evolution of NRPMw around merger is fully calibrated on NR data, while NRPM uses a post-Newtonian approximation. The quasiuniversal relations used in NRPM are not calibrated on SACRA data, although they are compatible with the new ones computed here for NRPMw. Moreover, NRPMw includes a full description of damped FM effects and it permits the calibration of the collapse time $t_{\rm coll}$, that improves the characterization of the f_2 peak.

In the following sections, we discuss the introduction of the recalibration parameters for both time- and frequency-domain models (Sec. VA) and we present the unfaithfulness results (Sec. VB) computed on the independent validation set of NR data.

A. Recalibrations

The EOS-insensitive relations developed in Sec. IV carry intrinsic uncertainties due to small violations of universality (EOS dependence) and/or fitting inaccuracies. Calibration errors of the empirical relations should be taken into account every time such mappings are employed, in particular during the calculation of fitting factors and during parameter estimation, in order to perform robust predictions. This can be done by introducing appropriate parameters associated with the fluctuation of the residuals. A byproduct of this process is that the model can improve its performance in describing the data.

Labeling Q a generic quantity estimated from a quasiuniversal relation calibrated on NR data, we introduce an associated *recalibration* δ_Q that affects the prediction $Q^{\rm fit}$ of the EOS-insensitive relation as

$$Q=Q^{\rm fit}(1+\delta_Q).\qquad(25)$$

The recalibration δ_Q corresponds to a fractional displacement from the prediction $Q^{\rm fit}$ of the quasiuniversal relation. The recalibration procedure employed here is similar to the spectral calibration envelopes used in GW analyses [116]. However, here we aim to integrate the model's uncertainties in the inference rather than the instrumental errors. A similar approach has been used in [18] (Sec. V).

In GW inference applications, the recalibrations of each calibrated PM property are treated as standard parameters. In this context, it is key that the prior distribution used in the inference is a good representation of the residuals of the EOS-insensitive relation. This allows us to perform a rigorous marginalization on the theoretical uncertainties of the model, delivering more robust and conservative estimates. Interestingly, under the assumption that the NR error is subdominant compared to the physical breaking of quasiuniversality, the measurement of the recalibration parameters from the data could also be used to distinguish between different EOSs and observatively probe the breaking of quasiuniversality.

A robust characterization of the NR errors is needed in order to employ a coherent prior distribution for the recalibration parameters in the GW inference routines.

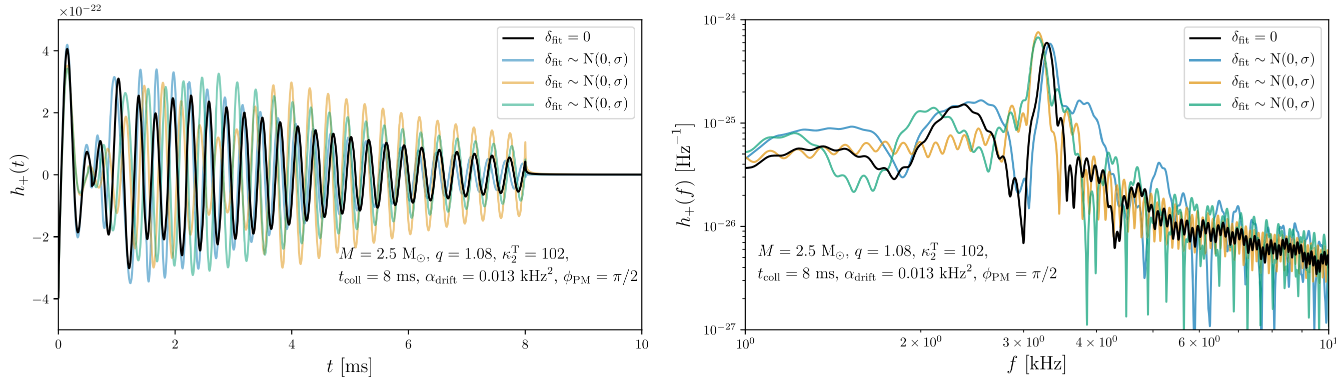

FIG. 4. Effect of recalibration terms on NRPMw waveform. The figures show exemplary templates of the GW plus polarization h_+ in the time domain (left) and in the frequency domain (right). The template has been computed for the parameters $M = 2.5M_\odot$, $q = 1.08$, $\kappa_2^T = 102$, $t_{\rm coll} = 8$ ms, $\alpha_{\rm peak} = 0.013$ kHz^2, $\phi_{\rm PM} = \pi/2$ and locating the source at a luminosity distance of 40 Mpc. Black lines show the exact NRPMw predictions, i.e. the recalibration parameters are identically zero, $\boldsymbol{\delta}_{\rm fit} = 0$. The colored lines show three exemplary cases where the values of the recalibrations $\boldsymbol{\delta}_{\rm fit}$ have been randomly extracted from a zero-mean normal distribution with variance prescribed by the errors of the residuals.

A priori, any prior with main support comparable to the span of know examples is a reasonable pragmatic choice. A more accurate approach would estimate the uncertainties associated to an EOS-insensitive relation as functions of the employed parameters using regressive methods or parameter estimation techniques. Following the methods of Refs. [18,116], an alternative and simpler approach is to consider a normally distributed prior distribution with variance prescribed by the errors of the residuals (see Table I).

Figure 4 illustrates the use of recalibrations in NRPMw for an examplary case. The recalibration parameters $\boldsymbol{\delta}_{\rm fit} = \{\delta_i\}$ are considered for each element of $\boldsymbol{\theta}_{\rm fit}$. These additional degrees of freedom mildly affect the merger portion, i.e. $t < t_0$ due to the accuracy of the empirical relations close to merger. However, the recalibration coefficients have a larger effect on the late-time PM features whose EOS-insensitive relations introduce larger uncertainties. Analogously, the recalibrations can be introduced for NRPM. This additional flexibility is expected to significantly improve the data fitting by adjusting the PM morphology of the template to match the targeted signal, similarly to agnostic approaches (e.g. [38,42]).

B. Unfaithfulness

We compare here the NR faithfulness results for NRPMw and NRPM. In Fig. 5, we report histograms of the unfaithfulness computed on the validation NR sample of

(i) NRPM without resorting to minimization methods;
(ii) NRPM minimizing over the additional PM parameters $\{\alpha, \beta, \phi_{\rm PM}\}$ and setting $\boldsymbol{\delta}_{\rm fit} = 0$;
(iii) NRPM with recalibration parameters $\boldsymbol{\delta}_{\rm fit}$ and minimizing over $\boldsymbol{\delta}_{\rm fit}$ and $\{\alpha, \beta, \phi_{\rm PM}\}$;
(iv) NRPMw minimizing over the additional PM parameters $\boldsymbol{\theta}_{\rm free}$ and setting $\boldsymbol{\delta}_{\rm fit} = 0$;
(v) NRPMw with recalibration parameters $\boldsymbol{\delta}_{\rm fit}$ and minimizing over $\boldsymbol{\delta}_{\rm fit}$ and $\boldsymbol{\theta}_{\rm free}$.

In particular, the minimization procedure is performed as follows. For each NR waveform, we compute the corresponding NRPMw (or NRPM) template fixing the intrinsic parameters $\boldsymbol{\theta}_{\rm bin}$ to the values of the NR simulation and estimating the additional parameters ($\boldsymbol{\theta}_{\rm free}$ and $\boldsymbol{\delta}_{\rm fit}$) minimizing the unfaithfulness $\bar{\mathcal{F}}$, i.e. Eq. (23), using a

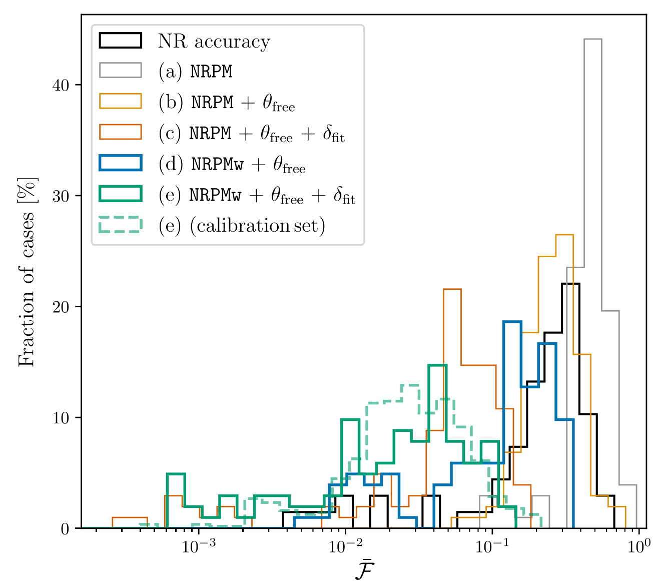

FIG. 5. Recovered unfaithfulness $\bar{\mathcal{F}}$ between PM models and NR data of the validation set [11,57,62,73,93,115] employing ET-D sensitivity [2,3]. For NRPM [11] (thin lines), we compute $\bar{\mathcal{F}}$ with the standard model (a), including PM parameters (b) and also the recalibrations (c). Analogously, the $\bar{\mathcal{F}}$ recovered for NRPMw (thick lines) include the PM parameters (d) and also the recalibrations (e). The dashed histogram shows the $\bar{\mathcal{F}}$ for case (e) computed over the calibration set.

differential evolution method [117]. For each case and for each NR data, the additional degrees of freedom are independently varied over a physically motivated range[7] in order to estimate the minimum $\bar{\mathcal{F}}$. If $t_{\rm coll}$ is such that some wavelet components are not included in the template, NRPMw does not depend on the related wavelet parameters; the latter are simply fixed by NR-calibrated relations or extracted from the prior. Moreover, Fig. 5 includes also the NR accuracy of the validation set (black line) computed as the unfaithfulness between low-resolution and high-resolution PM templates extracted from NR simulations with identical EOS and BNS parameters.

Case (i) gives results comparable to [11], with median value $\bar{\mathcal{F}}$ equal to 0.45 and few cases with $\bar{\mathcal{F}} \leq 0.1$ (2%). Indeed, the only differences between this work and Ref. [11] are the PSD and the different validation set. In case (ii), the inclusion of the free parameters $\{\alpha, \beta, \phi_{\rm PM}\}$ improves the faithfulness of NRPM by shifting the median value to $\bar{\mathcal{F}} \simeq 0.27$, but the majority of the recovered values (97%) lies above $\bar{\mathcal{F}} = 0.1$. The results of case (ii) show values comparable to NR accuracy. The additional inclusion of the recalibration parameters, shown in case (iii), considerably enhances the quality of the recovered waveforms, since $\bar{\mathcal{F}}$ decreases with median $\bar{\mathcal{F}} = 0.06$ and down to $\bar{\mathcal{F}} \sim O(10^{-3})$, corresponding to short-lived remnants and prompt BH collapses. The fraction of cases with $\bar{\mathcal{F}} < 0.1$ corresponds to 83% and we recovered $\bar{\mathcal{F}} < 0.2$ for all binaries in the validation set.

Moving to the novel NRPMw model, case (iv) show an overall improvement in the faithfulness compared to the equivalent case (ii), with median $\bar{\mathcal{F}} \sim 0.13$ and a fraction of 38% with $\bar{\mathcal{F}} < 0.1$. We attributed this enhancement to the modeling choices employed in NRPMw, since the number of parameters minimized ($\boldsymbol{\theta}_{\rm free}$) is the same as case (ii). Moreover, case (iv) shows a small cluster with $\bar{\mathcal{F}} \lesssim 3 \times 10^{-2}$ (~20%), mainly populated by short-lived remnant and prompt BH collapses. In case (v), the additional inclusion of recalibration terms considerably improves the agreement of NRPMw to the NR data. We obtain a median $\bar{\mathcal{F}}$ of 2.5×10^{-2} and report 94% of the validation set with $\bar{\mathcal{F}} < 0.1$. We recover similar statistics applying case (v) over the 600 NR simulations of the calibration set, shown with dashed line in Fig. 5. Moreover, the histogram (v) shows that the cluster constituted by short-duration signals moves toward $\bar{\mathcal{F}} = 10^{-2}$ and we recovered values comparable to or smaller than $\bar{\mathcal{F}} = 3 \times 10^{-2}$ for several long-duration transients, such as SLy $1.30 + 1.30 M_\odot$, and unequal-mass binaries, such as DD2 $1.50 + 1.25 M_\odot$. The overall improvement with respect to the comparable case (iii) is roughly half order of magnitude. The recovered results validate the modeling choices, suggesting that the primary contributions of the theoretical errors are the inaccurate predictions of the EOS-insensitive relations. Moreover, the majority of the recovered values lie below the NR accuracy threshold, representing an improvement with respect to the non-recalibrated scheme and validating the usage of NRPMw in practical data analysis. For some exemplary cases, we repeated the unfaithfulness computations varying the smoothness of the employed window function, finding absolute deviations of $O(10^{-3})$.

Considering the faithfulness condition proposed in Refs. [118–120] and fixing $N = 9$ as number of intrinsic parameters $\{\boldsymbol{\theta}_{\rm bin}, \boldsymbol{\theta}_{\rm free}\}$, the recovered upper-bound accuracy $\bar{\mathcal{F}} \simeq 10^{-1}$ of NRPMw in case (e) can be translated into a model robustness threshold of SNR ~ 7. Above this threshold, systematic waveform errors can become relevant. The threshold moves to SNR ~ 11 if we include the recalibrations $\boldsymbol{\delta}_{\rm fit}$ as intrinsic parameters, i.e. $N = 22$. On the other hand, employing the recovered median value $\bar{\mathcal{F}} \simeq 2.5 \times 10^{-2}$, we estimate a faithfulness threshold SNR equal to 13 for $N = 9$ and 21 for $N = 22$. Considering an averaged threshold of SNR ~ 10, this limit matches the requirements imposed by ET detector for (optimally oriented) sources located at luminosity distances $\gtrsim 40$ Mpc [11,17,41,42,121].

The $\bar{\mathcal{F}}$ values computed on simulations with different grid resolution or physical schemes suffer from considerable fluctuations for some binaries. Some examples are these: LS220 $1.47 + 1.27 M_\odot$ that gives $\log_{10} \bar{\mathcal{F}} = -0.84$ at standard resolution without turbulent viscosity and $\log_{10} \bar{\mathcal{F}} = -1.42$ at high resolution with turbulent viscosity; and LS220 $1.35 + 1.35 M_\odot$ (with turbulent viscosity) that gives $\log_{10} \bar{\mathcal{F}} = -1.05$ at standard resolution and $\log_{10} \bar{\mathcal{F}} = -1.79$ at low resolution. These results suggest that the largest $\bar{\mathcal{F}}$ might be related to an inaccurate modeling of the late-time features or to an excess of numerical error in the data. The accuracy of NR templates computed from different grid resolutions spans the range $\bar{\mathcal{F}} \simeq 0.6$ to $\bar{\mathcal{F}} \simeq 10^{-2}$ with a median value of ~0.25 (similarly to the results of Ref [11]). These non-negligible errors originate from finite resolution of numerical data. For the current knowledge (limited by number and accuracy of NR templates), NRPMw includes the necessary degrees of freedom required to match PM GW signals up to SNRs expected for next-generation detectors [5,17,122]. On the other hand, these results show that NRPMw can better reproduce the high-resolution NR data compared to the corresponding low-resolution NR template for a fixed combination of intrinsic BNS parameters. The unfaithfulness between different NR resolutions of $O(0.1)$ suggests that low-resolution NR templates provide inadequate representations of the GW signals and raises the necessity of more accurate NR templates.

[7]For NRPMw, we set the time of collapse $t_{\rm coll} \geq t_0$, the frequency drift $M^2 \alpha_{\rm peak} \in [-10^{-5}, 10^{-5}]$, the PM phase $\phi_{\rm PM} \in [0, 2\pi]$ and the recalibrations $\delta_i \in [-4\sigma_i, +4\sigma_i]$, where i runs over the calibrated PM quantities and σ_i is the corresponding standard deviation of the NR residuals (see Table I). The parameter space is uniformly sampled for all degrees of freedom.

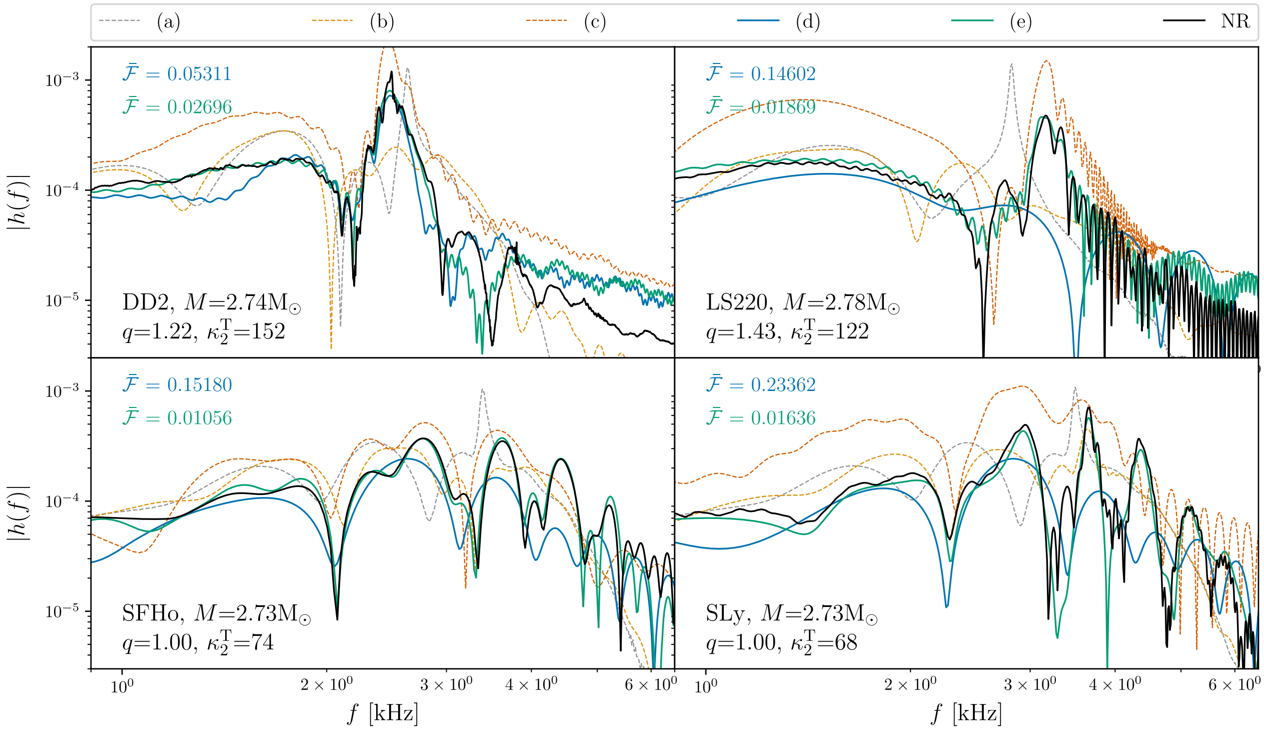

FIG. 6. Comparison between PM models and exemplary NR data of the validation set. Colored lines show the spectra for the different models, analogously to Fig. 5. Solid lines are used for NRPMw spectra and dashed lines are employed for NRPM. NR spectra are reported with black solid lines. The plot includes also the corresponding unfaithfulnesses estimated with NRPMw model, i.e. case (d) in blue and case (e) in green.

Figure 6 shows the comparison between the PM model spectra and NR data for four exemplary cases extracted from the validation set. The first case is DD2 $1.509 + 1.235 M_\odot$ which generates a long-lived remnant, $t_{coll} \sim O(100\ \text{ms})$. The NRPM model (i) predicts an erroneous f_2 peak, which biases the estimation of the damping time in case (ii). The result improves to $\log_{10} \bar{\mathcal{F}} = -1.3$ in case (iii). The novel NRPMw matches well the NR data, delivering $\log_{10} \bar{\mathcal{F}} = -1.3$ in case (iv) and $\log_{10} \bar{\mathcal{F}} = -1.6$ in case (v). The second case is LS220 $1.635 + 1.146 M_\odot$ with tidal-disruptive behavior that collapses into BH ~12 ms after merger. For this simulation, NRPMw (iv) is not capable to match the dominant PM peak returning $\bar{\mathcal{F}} \simeq 0.15$. Then, the recalibrations (v) strongly improve the agreement to NR data, yielding $\log_{10} \bar{\mathcal{F}} = -1.7$. The third case is SFHo $1.364 + 1.364 M_\odot$ which generates a short-lived remnant with $t_{coll} \simeq 4$ ms. This spectrum highlights the relevance of modulation effects in PM signals. The comparison shows the flexibility of the recalibrated NRPMw (v) in capturing the several Fourier peaks, delivering $\log_{10} \bar{\mathcal{F}} = -1.9$. The last case is SLy $1.364 + 1.364 M_\odot$ with $t_{coll} \simeq 12$ ms that shows prominent modulations in the spectrum. NRPM does not match well the prominent subdominant peaks returning $\log_{10} \bar{\mathcal{F}} = -0.7$ in case (iii). This result is similar to NRPMw (iv) but considerably improved with the inclusion of recalibrations (v) to $\log_{10} \bar{\mathcal{F}} = -1.8$.

VI. CONCLUSIONS

This paper presents NRPMw, a frequency-domain model for PM GW from BNS remnants calibrated with EOS-insensitive relations from the largest publicly-available set of NR simulations. NRPMw is designed to be employed in fully or partially informed Bayesian inference from GW data. NRPMw includes the dependency on the intrinsic binary parameters through the EOS-insensitive relations, thus allowing (i) the direct astrophysical inference of *all* the BNS parameters without assuming a premerger signal/detection, and at the same time (ii) a phase-coherent attachment with premerger templates [11]. The current uncertainties of EOS-insensitive relations can be taken into account in a partially informed approach using recalibrations parameters. This enhances the flexibility of the model in capturing the complex morphology of PM signals and improves fitting factors. We stress that a recalibration procedure similar to the one introduce here should be employed every time EOS insensitive are applied to any type of data.

NRPMw was validated with an independent set of 102 NR simulations. The fitting factors favorably compares against the results obtained with similar frequency-domain models [41] and significantly improve those we obtained with NRPM [11]. The improvement is mainly related to a more accurate modeling of the *merger* features and to an improved description of the FMs when compared to NRPM. The faithfulness of the recalibrated NRPMw is comparable to that obtained using unmodeled (noninformed) templates and agnostic approaches [42,43]. This comes at the cost of 13 recalibration parameters and three free parameters, compared to the typical $O(10)$ parameters of unmodeled templates. However, differently from the latter, NRPMw delivers complete posteriors for the BNS parameters, including mass, mass ratio, etc. The NRPMw faithfulnesses are comparable to the accuracy of current NR templates for BNS remnants. The further development of high-precision NR simulations is key for the design of robust PM models.

NRPMw builds on a new set of EOS-insensitive relations for the PM spectra. We have focused the development of quasiuniversal relation that employ the tidal coupling constant κ_2^{T} in view of utilizing the model as an EOB completion [10,11,113,114]. The most robust relations we obtained are, not surprisingly, the merger amplitude, the merger frequency and the dominant f_2 peak. The $1-\sigma$ uncertainties of these relations are of the order of 4% due to either uncertainties of NR data or EOS-dependent features. The use of dimensionless and mass-rescaled quantities is a key aspect in building EOS-insensitive relations. An example illustrating this fact is the breaking of the quasiuniversal relations claimed in Ref. [123]. The latter refers to relations of type $f_2(R)$ that are different from those employed here. In Appendix F, we verified that those $f_2(R)$ relations are broken also by some data of the CORE database. The additional term proposed in [123] does not fix the breaking of some CORE data with softening effects at high densities. However, we verified that the use of mass-rescaled quantities, i.e. $Mf_2(R/M)$, leads to more robust EOS-insensitive relations. Hence, considering $Mf_2(R/M)$ or $f_2(R)$ in a Bayesian analysis of the same data would incorrectly lead to two different conclusions about the EOS.

We found that the presence of softening effects due to quark deconfinement or hyperonic degrees of freedom at high densities does *not* introduce significant deviations above the $2-\sigma$ credibility level in the EOS-insensitive relation for f_2 developed here. Hence, the observational imprint of EOS softening might be better revealed from an earlier BH collapse phenomenology, e.g. [16,25,87,124,125], rather than from the measurement of PM frequencies (under the assumption that our sample of models adequately represent the "true" EOS). However, the cases BHB$\Lambda\phi$ $1.50+1.50M_\odot$, BLQ $1.40+1.40M_\odot$[8] and other literature results [26,126,127] suggest that the EOS-insensitive relations for $Mf_2(\kappa_2^{\mathrm{T}})$ (and in principle for other quantities) might break for particular binary masses and in presence of "strong" phase transitions.[9] This opens the possibility of using NRPMw to identify this new extreme matter physics via Bayesian analyses following the method of [11,44]. We stress that these types of analyses strictly probe only the violation of the particular quasiuniversal relation that is assumed in a model. Hence, the robust construction of EOS-insensitive relations and the use of recalibration parameters are key for the interpretation of the inference results. Future analysis must incorporate the here proposed recalibration parameters in the inference, because assessing the breaking of the quasiuniversality requires the knowledge of the theoretical uncertainty of the EOS-insensitive relation.

In paper II [19], we report a study on the application of NRPMw to detection and Bayesian parameter estimation of mock PM signal with ET and we will discuss full-spectrum BNS analyses in a third paper of this series. In this regard, the employment of recalibration parameters $\boldsymbol{\delta}_{\mathrm{fit}}$ is essential also in the context of Bayesian inference since they improve the agreement of NRPMw to NR data below their threshold accuracy, as discussed in Sec. V. As anticipated by the faithfulness calculations presented here, NRPMw can improve the performances of NRPM [11], yielding to threshold SNRs comparable to those of unmodeled analyses [38,42]. For example, the model can be used to infer the dynamical frequency evolution of the remnant and the time of BH collapse already at the minumum SNR treshold. Under the important caveat on the robusteness of the assumed EOS-insensitive relations discussed above, these observables can provide insight into the properties of matter under extreme conditions and prove breaking of quasiuniversality. Moreover, NRPMw can be employed together with inspiral-merger templates to characterize the full GW spectrum of BNS mergers and improve the EOS constraints [11,17].

The waveform model developed in this work, NRPMw, is implemented in BAJES and the software is publicly available at [128].

ACKNOWLEDGMENTS

M. B., S. B. and K. C. acknowledge support by the EU H2020 under ERC Starting Grant No. BinGraSp-714626. M. B. acknowledges support from the Deutsche Forschungsgemeinschaft (DFG) under Grant No. 406116891 within the Research Training Group RTG 2522/1. S. B. acknowledges the hospitality of KITP at UCSB and partial support by the National Science Foundation under Grant No. NSF PHY-1748958 during

[8]As discussed in Sec. IV B, these massive binaries of Refs. [11,16,25] are marginal cases very close to prompt collapse and its interpretation is not fully clear with the present data.

[9]The term "strong" is often used in the literature but it does not have any precise meaning; in this context it is used as a tautology to indicate that the EOS model breaks the quasiuniversal relation.

the conclusion of this work. A. C. and A. P. acknowledge PRACE for awarding them access to Joliot-Curie at GENCI@CEA. They also acknowledge the usage of computer resources under a CINECA-INFN agreement (allocation INF20_teongrav and INF21_teongrav). The computations were performed on ARA, a resource of Friedrich-Schiller-Universtät Jena supported in part by DFG Grants No. INST 275/334-1 FUGG, No. INST 275/363-1 FUGG and No. EU H2020 BinGraSp-714626 and on the TULLIO sever at INFN Turin.

APPENDIX A: WAVELET APPROXIMATIONS

We discuss the approximations employed to compute the frequency-domain wavelet $W(f)$ Eq. (8) for different values of the α parameter.

When α is identically zero, Eq. (7) reduces to a damped sinusoidal function, but Eq. (8) leads to an indeterminate form. Then, the latter can be replaced by

$$W(f) = \mathrm{e}^{\gamma}\left(\frac{\mathrm{e}^{\tau\zeta}-1}{\zeta}\right), \tag{A1}$$

where $\zeta(f) = \beta - 2\pi\mathrm{i}f$. Equation (A1) represents a good approximation also when the wavelet is strongly damped, i.e. $\Re(\beta)$ dominates over the quadratic contributions. This is crucial to simplify the computations for higher-order FM terms, whose damping time decrease linearly with the approximation order (see Appendix B).

For $|\alpha| \ll 1$, arithmetic overflows arise in numerical computations. Then, for these cases, we expand Eq. (7) around small values of αt^2, i.e.

$$W(t) = \mathrm{e}^{\beta t+\gamma}\sum_{n=0}^{\infty}\frac{(\alpha t^2)^n}{n!}. \tag{A2}$$

Each term in Eq. (A2) can be analytically integrated, leading to a well-defined solution of the Fourier counterpart. In particular,

$$W(f) = \mathrm{e}^{\gamma}\sum_{n=0}^{\infty}\int_0^{\tau}\frac{(\alpha t^2)^n}{n!}\mathrm{e}^{(\beta-2\pi\mathrm{i}f)t}\mathrm{d}t, \tag{A3}$$

from which it follows

$$W(f) = \frac{\mathrm{e}^{\gamma}}{\sqrt{\pi}}\sum_{n=0}^{\infty}(4\alpha)^n\Gamma\left(n+\frac{1}{2}\right)\frac{G_{2n}(-\zeta\tau)-1}{\zeta^{2n+1}}, \tag{A4}$$

where $\Gamma(n)$ is the gamma function and $G_n(x)$ corresponds to

$$G_n(x) = \mathrm{e}^{-x}\sum_{k=0}^{n}\frac{x^k}{k!}. \tag{A5}$$

We observe that $G_n \to 1$ for $n \to \infty$. Limiting the series to $n = 0$, Eq. (A4) leads to the damped sinusoidal case, i.e. Eq. (A1). In our implementation, we use Eq. (A4) as approximation of $W(f)$ for $|\alpha|\tau^2 \lesssim 0.1$ accounting up to $n = 4$.

APPENDIX B: FM APPROXIMATION

In this appendix, we discuss the approximation performed in order to reach an analytical form for the FM effects in terms of $W(f)$, i.e. Eq. (8).

Let us start considering a generic nonmodulated wavelet $W(t)$, as the one in Eq. (7). This term can be decomposed in amplitude and phase, analogously to Eq. (2), from which we can compute the frequency, that reads

$$\omega_W(t) = -2\Im(\alpha)t - \Im(\beta). \tag{B1}$$

In order to include damped FMs, we generalize the notion of W introducing $\tilde{W}$, such that

$$\omega_{\tilde{W}}(t) = \omega_W(t) - \Delta_{\mathrm{fm}}\mathrm{e}^{-\Gamma_{\mathrm{fm}}t}\sin(\Omega_{\mathrm{fm}}t+\phi_{\mathrm{fm}}), \tag{B2}$$

where $\Delta_{\mathrm{fm}}, \Gamma_{\mathrm{fm}}, \Omega_{\mathrm{fm}}, \phi_{\mathrm{fm}} \in \mathbb{R}$ define the modulation, i.e. the frequency displacement $\Delta_{\mathrm{fm}} \geq 0$, the inverse damping time Γ_{fm}, the modulation frequency Ω_{fm} and the initial phase ϕ_{fm}. Integrating Eq. (B2), the frequency-modulated wavelet $\tilde{W}(t)$ can be rewritten in the time domain as

$$\tilde{W}(t) = W(t;\alpha,\beta,\gamma,\tau)\mathrm{e}^{-\mathrm{i}F(t;\Delta_{\mathrm{fm}},\Gamma_{\mathrm{fm}},\Omega_{\mathrm{fm}},\phi_{\mathrm{fm}})}, \tag{B3}$$

where $F(t)$ corresponds to

$$F(t) = \frac{\Delta_{\mathrm{fm}}\mathrm{e}^{-\Gamma_{\mathrm{fm}}t}}{\Gamma_{\mathrm{fm}}^2+\Omega_{\mathrm{fm}}^2}[\Gamma_{\mathrm{fm}}\sin(\Omega_{\mathrm{fm}}t+\phi_{\mathrm{fm}}) + \Omega_{\mathrm{fm}}\cos(\Omega_{\mathrm{fm}}t+\phi_{\mathrm{fm}})] - F_0, \tag{B4}$$

with

$$F_0 = \frac{\Delta_{\mathrm{fm}}}{\Gamma_{\mathrm{fm}}^2+\Omega_{\mathrm{fm}}^2}(\Gamma_{\mathrm{fm}}\sin\phi_{\mathrm{fm}}+\Omega_{\mathrm{fm}}\cos\phi_{\mathrm{fm}}). \tag{B5}$$

Notice that $F(t) \in \mathbb{R}$ and $\mathrm{e}^{-\mathrm{i}F(t)}$ is a unitary complex factor for every given t.

Due to the oscillatory nature of $F(t)$, the frequency-domain wavelet $\tilde{W}(f)$ cannot be analytically computed using Gaussian integration rules. Then, we rewrite $F(t)$ in terms of exponential functions,

$$F(t) = \frac{\mathrm{i}\Delta_{\mathrm{fm}}}{2|\beta_{\mathrm{fm}}|^2}(\beta_{\mathrm{fm}}^*\mathrm{e}^{-\beta_{\mathrm{fm}}t-\mathrm{i}\phi_{\mathrm{fm}}} - \beta_{\mathrm{fm}}\mathrm{e}^{-\beta_{\mathrm{fm}}^*t+\mathrm{i}\phi_{\mathrm{fm}}}) - F_0, \tag{B6}$$

where $\beta_{\mathrm{fm}} = \Gamma_{\mathrm{fm}} + \mathrm{i}\Omega_{\mathrm{fm}}$. Subsequently, we expand the exponential $\mathrm{e}^{-\mathrm{i}F}$, i.e.

$$e^{-iF(t)} = \sum_{n=0}^{\infty} \frac{[-iF(t)]^n}{n!}. \tag{B7}$$

Combining Eqs. (B3), (B6) and (B7), we can write $\tilde{W}(t)$ in terms of $W(t)$ and perform an analytical Fourier transform. In particular,

$$\tilde{W}(f) = e^{iF_0} \sum_{n=0}^{\infty} \left(\frac{\Delta_{\rm fm}}{2|\beta_{\rm fm}|^2} \right)^n \frac{w_n(f)}{n!}, \tag{B8}$$

where

$$w_n(f) = \sum_{k=0}^{n} \binom{n}{k} (\beta^*_{\rm fm})^k (-\beta_{\rm fm})^{n-k} W(f; \alpha, \beta_{n,k}, \gamma_{n,k}, \tau), \tag{B9}$$

with

$$\begin{aligned} \beta_{n,k} &= \beta - k\beta_{\rm fm} - (n-k)\beta^*_{\rm fm}, \\ &= \beta - n\Gamma_{\rm fm} + i(n-2k)\Omega_{\rm fm}, \\ \gamma_{n,k} &= \gamma_{\rm fm} + i(n-2k)\phi_{\rm fm}. \end{aligned} \tag{B10}$$

and $\{\alpha, \beta, \gamma, \tau\}$ are the parameters of the corresponding nonmodulated wavelet.

Equation (B8) generates several Fourier contributions centered around the frequencies $\Im(\beta) \pm n\Omega$, as expected from FM effects. A second order approximation gives good agreement for small modulation indices, i.e. $\Delta/\Omega \ll 1$; however, when Δ is comparable to Ω, additional terms need to be taken into account for an accurate description. The maximum order of approximation $n_{\rm max}$ is estimated using an empirical rule of thumb, $n_{\rm max} \approx 2(1 + \Delta/\Omega)$.

APPENDIX C: CHOICES FOR WAVELET COMPOSITION

The first contribution, $W_{\rm fus}$, corresponds to the fusion of the NS cores. This term is modeled with a Gaussian wavelet (i.e. $i\beta \in \mathbb{R}$), with initial amplitude, frequency and phase defined by the values at merger, respectively $A_{\rm mrg}$, $f_{\rm mrg}$ and $\phi_{\rm mrg}$. The width of the amplitude is fixed as follows:

$$\Re(\alpha_{\rm fus}) = \frac{\log(A_0/A_{\rm mrg})}{t_0^2}, \tag{C1}$$

while the frequency slope $\Im(\alpha_{\rm fus})$ is directly estimated from NR data. The fusion wavelet $W_{\rm fus}$ is truncated at t_0. It follows that

$$\begin{aligned} W_{\rm fus}(f) = W(f; \alpha &= \Re(\alpha_{\rm fus}) - i\Im(\alpha_{\rm fus}), \\ \beta &= -2\pi i f_{\rm mrg}, \\ \gamma &= \log(A_{\rm mrg}) - i\phi_{\rm mrg}, \\ \tau &= t_0, \\ \tau_0 &= 0). \end{aligned} \tag{C2}$$

Subsequently, we include an intermediate wavelet $\tilde{W}_{\rm bnc}$ that characterizes the bounce of the remnant after the collision of the NS cores, corresponding to the time interval $[t_0, t_1]$. The initial amplitude is determined in order to match the A_0 and the phase is computed from the wavelet $W_{\rm fus}$ including an additional phase shift $\phi_{\rm PM}$, shown by NR simulations [78,88], i.e.

$$\phi_{\rm bnc} = \phi_{\rm mrg} + \phi_{\rm PM} + 2\pi f_{\rm mrg} t_0 + \Im(\alpha_{\rm fus}) t_0^2. \tag{C3}$$

The amplitude coefficients, $\Re(\alpha_{\rm bnc})$ and $\Re(\beta_{\rm bnc})$, are chosen such that the amplitude peaks in the first local amplitude maximum, i.e. t_1, with value A_1:

$$\Re(\alpha_{\rm bnc}) = \frac{\log(A_0/A_1)}{(t_1 - t_0)^2}, \tag{C4}$$

$$\Re(\beta_{\rm bnc}) = \frac{2\log(A_1/A_0)}{t_1 - t_0}. \tag{C5}$$

The frequency is kept constant with value $\Im(\beta_{\rm bnc}) = -2\pi i f_2$. Then, including FM effects as discussed in Sec. III B, we get

$$\begin{aligned} \tilde{W}_{\rm bnc}(f) = W(f; \alpha &= \Re(\alpha_{\rm bnc}), \\ \beta &= \Re(\beta_{\rm bnc}) - 2\pi i f_2, \\ \gamma &= \log(A_0) - i\phi_{\rm bnc}, \\ \tau &= t_1 - t_0, \\ \tau_0 &= t_0, \\ \Delta_{\rm fm} &= \Delta_{\rm fm}, \\ \Gamma_{\rm fm} &= 0, \\ \Omega_{\rm fm} &= 2\pi f_0, \\ \phi_{\rm fm} &= \phi_{\rm fm}). \end{aligned} \tag{C6}$$

After t_1, the remnant is strongly deformed and the quadrupolar radiation is affected by couplings with subdominant modes, that introduce AMs. Physically, this phenomenon can be naively interpreted with the presence of radial pulsation in the mass distribution of the remnant object [23]. We limit ourselves to the modeling of AMs in the region $[t_1, t_3]$ taking into account the coupling with the (2,0) mode, analogously to Ref. [11]. This pulsating portion of signal can be approximated using a wavelet $\tilde{W}_{\rm pul}$ of the form,

$$\tilde{W}_{\rm pul}(t) = A_1[1-\Delta_{\rm am}\sin^2(\pi f_0 t)]\mathrm{e}^{[\Re(\beta_{\rm pul})-2\pi\mathrm{i}f_2]t-\mathrm{i}\phi_{\rm pul}}, \tag{C7}$$

where the initial amplitude and phase are chosen to match values of $\tilde{W}_{\rm bnc}$ at t_1, in particular the phase $\phi_{\rm pul}$ corresponds to

$$\phi_{\rm pul} = \phi_{\rm bnc} + 2\pi f_2(t_1 - t_0), \tag{C8}$$

the coefficient $\Re(\beta_{\rm pul})$ is defined by the amplitudes $A_{1,3}$ as

$$\Re(\beta_{\rm pul}) = \frac{\log(A_3/A_1)}{t_3 - t_1}, \tag{C9}$$

and the coefficient $\Delta_{\rm am}$ defines the magnitude of AMs,

$$\Delta_{\rm am} = 1 - \frac{A_2}{A_1}\left(\frac{A_1}{A_3}\right)^{\frac{t_2-t_1}{t_3-t_1}} = 1 - \frac{A_2}{\sqrt{A_1 A_3}}, \tag{C10}$$

where we made use of the definition of t_i (Sec. III A) in the second equality. Then, Eq. (C7) can be rewritten in terms of frequency-domain wavelets, Eq. (8), as

$$\begin{aligned}
\tilde{W}_{\rm pul}(f) = \left(1-\frac{\Delta_{\rm am}}{2}\right)W(f;\alpha = 0,\\
&\beta = \Re(\beta_{\rm pul}) - 2\pi\mathrm{i}f_2,\\
&\gamma = \log(A_1) - \mathrm{i}\phi_{\rm pul},\\
&\tau = t_3 - t_1,\\
&\tau_0 = t_1,\\
&\Delta_{\rm fm} = \Delta_{\rm fm},\\
&\Gamma_{\rm fm} = \Gamma_{\rm fm},\\
&\Omega_{\rm fm} = 2\pi f_0,\\
&\phi_{\rm fm} = \phi_{\rm fm})\\
+\frac{\Delta_{\rm am}}{4}W(f;\alpha = 0,\\
&\beta = \Re(\beta_{\rm pul}) - 2\pi\mathrm{i}(f_2 - f_0),\\
&\gamma = \log(A_1) - \mathrm{i}\phi_{\rm pul},\\
&\tau = t_3 - t_1,\\
&\tau_0 = t_1,\\
&\Delta_{\rm fm} = \Delta_{\rm fm},\\
&\Gamma_{\rm fm} = \Gamma_{\rm fm},\\
&\Omega_{\rm fm} = 2\pi f_0,\\
&\phi_{\rm fm} = \phi_{\rm fm})\\
+\frac{\Delta_{\rm am}}{4}W(f;\alpha = 0,\\
&\beta = \Re(\beta_{\rm pul}) - 2\pi\mathrm{i}(f_2 + f_0),\\
&\gamma = \log(A_1) - \mathrm{i}\phi_{\rm pul},\\
&\tau = t_3 - t_1,\\
&\tau_0 = t_1,\\
&\Delta_{\rm fm} = \Delta_{\rm fm},\\
&\Gamma_{\rm fm} = \Gamma_{\rm fm},\\
&\Omega_{\rm fm} = 2\pi f_0,\\
&\phi_{\rm fm} = \phi_{\rm fm}).
\end{aligned} \tag{C11}$$

Subsequently, we model the signal with a damped tail related to the quadrupolar deformations of the rotating remnant. The corresponding wavelet $\tilde{W}_{\rm peak}$ is modeled in the range $[t_3, t_{\rm coll}]$. If the remnant is a stable NS configuration, then $t_{\rm coll}\to\infty$. The initial amplitude and phase are chosen to match the values of $\tilde{W}_{\rm pul}$ at t_3,

$$\phi_{\rm peak} = \phi_{\rm pul} + 2\pi f_2(t_3 - t_1), \tag{C12}$$

$$A_{\rm peak} = A_3. \tag{C13}$$

The frequency evolution is characterized by the typical f_2 peak, i.e. $\Im(\beta_{\rm peak}) = -2\pi f_2$, with a nonvanishing slope $\Im(\alpha_{\rm peak})$ (also referred as $\alpha_{\rm peak}$ in the manuscript to lighten the notation). Then,

$$\begin{aligned}
\tilde{W}_{\rm peak}(f) = W(f;\alpha = -\mathrm{i}\Im(\alpha_{\rm peak}),\\
&\beta = \Re(\beta_{\rm peak}) - 2\pi\mathrm{i}f_2,\\
&\gamma = \log(A_3) - \mathrm{i}\phi_{\rm peak},\\
&\tau = t_{\rm coll} - t_3,\\
&\tau_0 = t_3,\\
&\Delta_{\rm fm} = \Delta'_{\rm fm},\\
&\Gamma_{\rm fm} = \Gamma_{\rm fm},\\
&\Omega_{\rm fm} = 2\pi f_0,\\
&\phi_{\rm fm} = \phi_{\rm fm}),
\end{aligned} \tag{C14}$$

where $\Delta'_{\rm fm} = \Delta_{\rm fm}\exp[\Gamma_{\rm fm}(t_3 - t_1)]$.

When $t_{\rm coll}$ is finite and the remnant collapse into BH, NR simulations show an increasing frequency and a damping amplitude similarly to a BH ringdown. This evolution can be captured with the inclusion of an additional wavelet component, i.e. $W_{\rm coll}$. However, this contribution is expected to be relatively weak in terms of GW luminosity with respect to the previous dynamics [24]. Moreover, the characteristic BH frequencies for this kind of systems lie in a very high frequency range, roughly $\gtrsim 6$ kHz [83], where the sensitivities of the detectors are generally poor. It follows that the collapse portion of the signal is expected to have negligible effect on the overall GW power and, for these reasons, we approximate $W_{\mathrm{coll}} = 0$.

The overall model includes 17 parameters: the merger amplitude A_{mrg} and frequency f_{mrg}; the frequency drift at merger $\Im(\alpha_{\mathrm{fus}})$; the characteristic PM frequencies f_2 and f_0; the frequency drift $\Im(\alpha_{\mathrm{peak}})$ (or α_{peak}); the time of the first nodal point t_0 and the corresponding phase shift ϕ_{PM}; the amplitude values at the different nodal points $\{A_i\}$, for $i = 0, 1, 2, 3$; the inverse damping time of the Lorentzian tail $\Im(\beta_{\mathrm{peak}})$; the time of collapse t_{coll}; and the FM properties, i.e. Δ_{fm} and Γ_{fm} and ϕ_{fm}. Finally, we observe that $\tilde{W}_{\mathrm{bnc}}(f)$, $\tilde{W}_{\mathrm{pul}}(f)$ and $\tilde{W}_{\mathrm{peak}}(f)$ are chosen to be identically zero for $\Lambda_1 = \Lambda_2 = 0$.

APPENDIX D: VISCOSITY IMPACT ON FREQUENCY DRIFT

In this Appendix, we show the effects of different viscosity schemes on the dynamical evolution of the GW frequency. This discussion aims to motivate the introduction of the frequency drift α_{peak} as free parameter.

Figure 7 shows three NR simulations extracted from [62,115] and computed with identical grid resolution. The data correspond to a BNS system with $M = 2.7 M_{\odot}$ and $q = 1$ with matter properties described by the same EOS, i.e. LS220 [102]. Moreover, all cases include neutrino reabsorption scheme [129]. The blue curves refer to binaries with no turbulent viscosity. The orange and green curves include turbulent viscosity with a fixed mixing length respectively equal to $\ell_{\mathrm{mix}} = 5$ m and $\ell_{\mathrm{mix}} = 25$ m. The mixing length ℓ_{mix} represents the characteristic scale over which turbulence acts [115]. Finally, the purple data are simulated with a turbulent viscosity scheme calibrated on high-resolution magneto-hydro-dynamical simulations of BNS mergers [130].

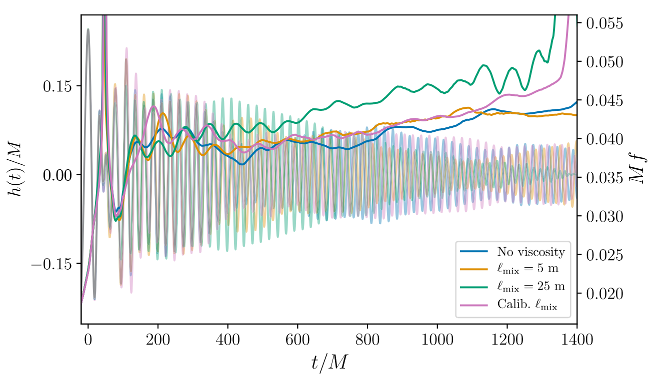

FIG. 7. GW data extracted from NR simulations with neutrino reabsorption of a BNS merger with $M = 2.7 M_{\odot}$, $q = 1$ and LS220 EOS [62,115]. Blue curve refers to data with no turbulent viscosity, orange curve refer to fixed $\ell_{\mathrm{mix}} = 5$ m, green curve refers to fixed $\ell_{\mathrm{mix}} = 25$ m and purple curve refers to ℓ_{mix} calibrated on [130]. Solid lines show the GW frequency Mf and shaded lines show the GW waveform h/M. The instant $t = 0$ corresponds to the merger.

Over the domain $t/M \lesssim 300$, the different cases show a similar behavior. However, for later times, the frequency drift significantly differs, with a more pronounced slope for the $\ell_{\mathrm{mix}} = 25$ m case. The same binary is the one that shows the earliest BH collapse. Notably, as shown in [115], the frequency slope is softer for $\ell_{\mathrm{mix}} = 50$ m with respect to the $\ell_{\mathrm{mix}} = 25$ m case; however, the assumption $\ell_{\mathrm{mix}} = 50$ m appears to be physically disfavored from studies of magnetorotational instability turbulence in BNS simulations [130]. On the other hand, the simulation with calibrated ℓ_{mix} shows an initial trend similar to the $\ell_{\mathrm{mix}} = 5$ m case; later, for $t/m \gtrsim 1000$, the two GW frequencies differ and the calibrated-viscosity case shows a BH collapse. Interestingly, the binaries with the steepest frequency drifts tend to generate shorter GW bursts due to earlier BH collapse. These physical effects cannot be described by the binary properties only (i.e. masses, spins and tides). Thus, it is necessary to rely on additional coefficients that aim to characterize the physical information on the matter dynamics encoded in the PM transients.

APPENDIX E: ADDITIONAL PARAMETERS FOR NRPM

In [17] and in Sec. V B, we introduced the additional parameters $\{\alpha, \beta, \phi_{\mathrm{PM}}\}$ for the NRPM model [11]. This Appendix aims to expand this discussion, specifying the role of each term with reference to [11].

The additional phase ϕ_{PM} affects the phase evolution of NRPM introducing a phase discontinuity in t_0, as previously discussed for NRPMw. The damping time α, defined in Eq. (11) of [11], is promoted to additional parameter, since it improves the fitting of the characteristic peak for NRPM. This is also motivated by the relation between the time of collapse and the high-density EOS properties [16,25,87]. Finally, the β parameter is inspired by the template model introduced in [42] and it takes into account linear deviations from the peak frequency f_2. In particular, it modifies Eq. (7d) of [11] as

$$\hat{\omega}(\hat{t} > \hat{t}_3) = \hat{\omega}_2 \cdot [1 + \beta(\hat{t} - \hat{t}_3)]. \quad \text{(E1)}$$

As discussed for NRPMw and in Appendix D, general PM GW transients show nonvanishing frequency slope and this feature appears to correlate with the viscosity scheme employed in the NR simulation.

APPENDIX F: QUASIUNIVERSAL RELATIONS OF TYPE $f_2(R)$

In this appendix, we discuss the quasiuniversal relations between the PM peak frequency f_2 and the NS radius at fiducial values in light of the results of [27,123]. In particular, we calibrate the relations $f_2(R_{1.4})$ and $f_2(R_{1.8})$ including the CORE data [16,57,62,73,88], where $R_{1.4}$ ($R_{1.8}$)

TABLE II. Summary of the calibrated relations for the PM peak frequency f_2 as function of the NS radii $R_{1.4}$ and $R_{1.8}$. The first column shows the calibrated quantity of interest; the calibrated values of the empirical coefficients are reported from the second to the fifth column.

$Q^{\rm fit}$	a_0	a_1	a_2	a_3
$f_2(R_{1.4})$	5.42	0.0449	−0.0198	…
$f_2(R_{1.8})$	11.5	−0.990	0.0233	…
$Mf_2(R_{1.4}/M)$	0.2	−0.0762	0.0078	…
$Mf_2(R_{1.8}/M)$	0.236	−0.103	0.0125	…
$f_2(R_{1.4}, R_{1.4}/R_{1.8})$	6.4	−1.33	0.0381	6.97
$f_2(R_{1.8}, R_{1.4}/R_{1.8})$	9.99	−1.24	0.0349	2.76
$Mf_2(R_{1.4}/M, R_{1.4}/R_{1.8})$	0.162	−0.115	0.0145	0.0919
$Mf_2(R_{1.8}/M, R_{1.4}/R_{1.8})$	0.213	−0.105	0.013	0.0241

is the radius of a $1.4M_\odot$ ($1.8M_\odot$) NS computed from the TOV equations.

Following [123], we employ a quadratic relation for the calibration of the PM peak as function of the NS radius, including linear corrections in the ratio $R_{1.4}/R_{1.8}$, i.e.

$$f_2(R_X) = a_0 + a_1 R_X + a_2 R_X^2, \tag{F1}$$

$$f_2\left(R_X, \frac{R_{1.4}}{R_{1.8}}\right) = a_0 + a_1 R_X + a_2 R_X^2 + a_3 \frac{R_{1.4}}{R_{1.8}}, \tag{F2}$$

for $X = 1.4$, 1.8, where f_2 is measured in kHz and R_X in km. Subsequently, we fit the NR data scaling the calibrated quantities by the total mass M of the system, i.e. $f_2 \mapsto Mf_2$ and $R_X \mapsto R_X/M$. Our final calibration set is composed by 65% by binaries with $R_{1.4}/R_{1.8} > 1$. Table II shows the

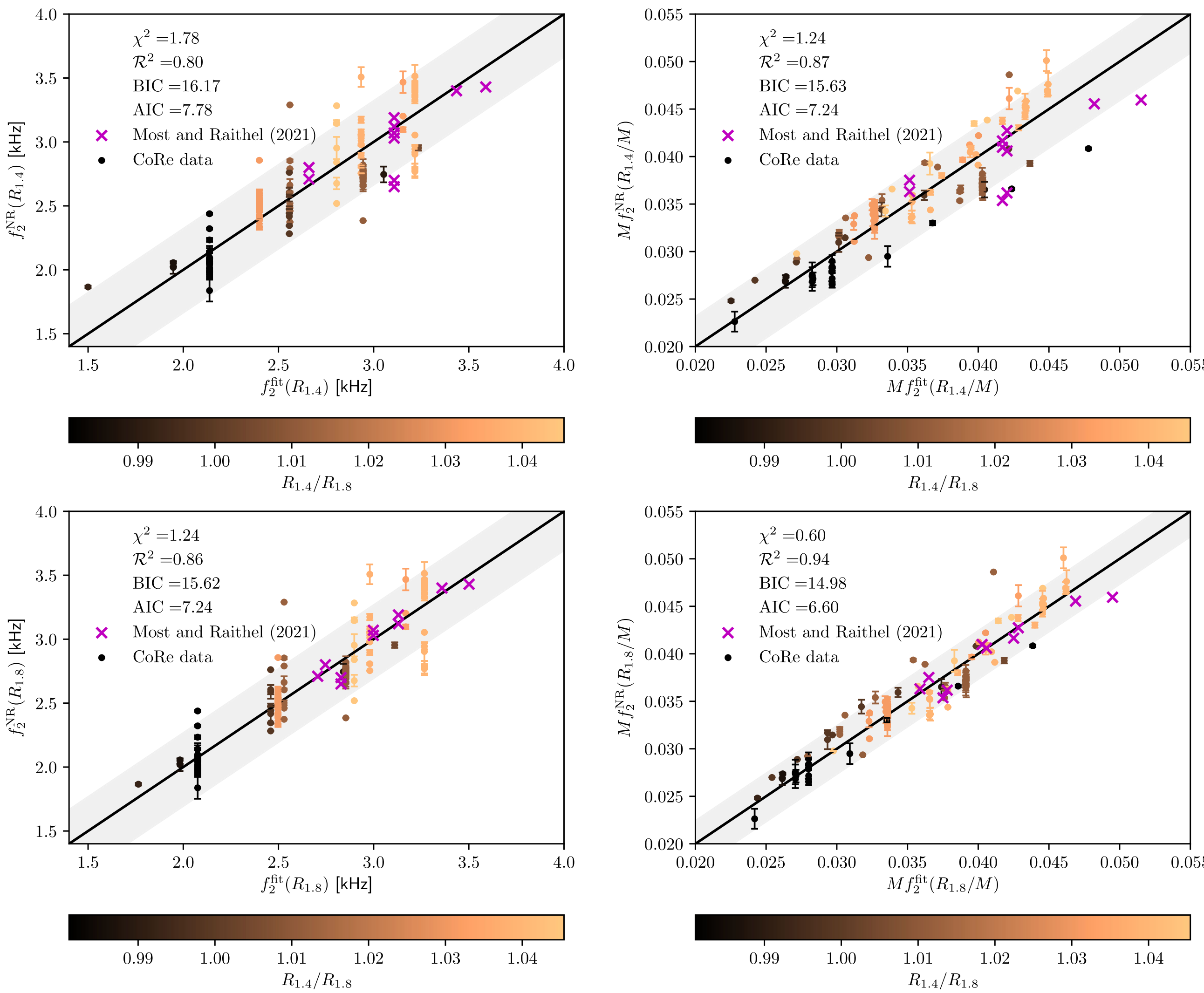

FIG. 8. Predicted values from the calibrated relations Eq. (F1) compared to the respective NR observed quantities. Top panels show $X = 1.4$ and bottom panels show $X = 1.8$. Left panels show non-mass-scaled f_2 and right panels show mass-scaled dimensionless Mf_2. The diagonal (black line) represents the case in which predictions and observations match and the gray area is the 90% credibility level. The CORE data are reported with circles colored according to $R_{1.4}/R_{1.8}$ and magenta crosses are the data extracted from [27].

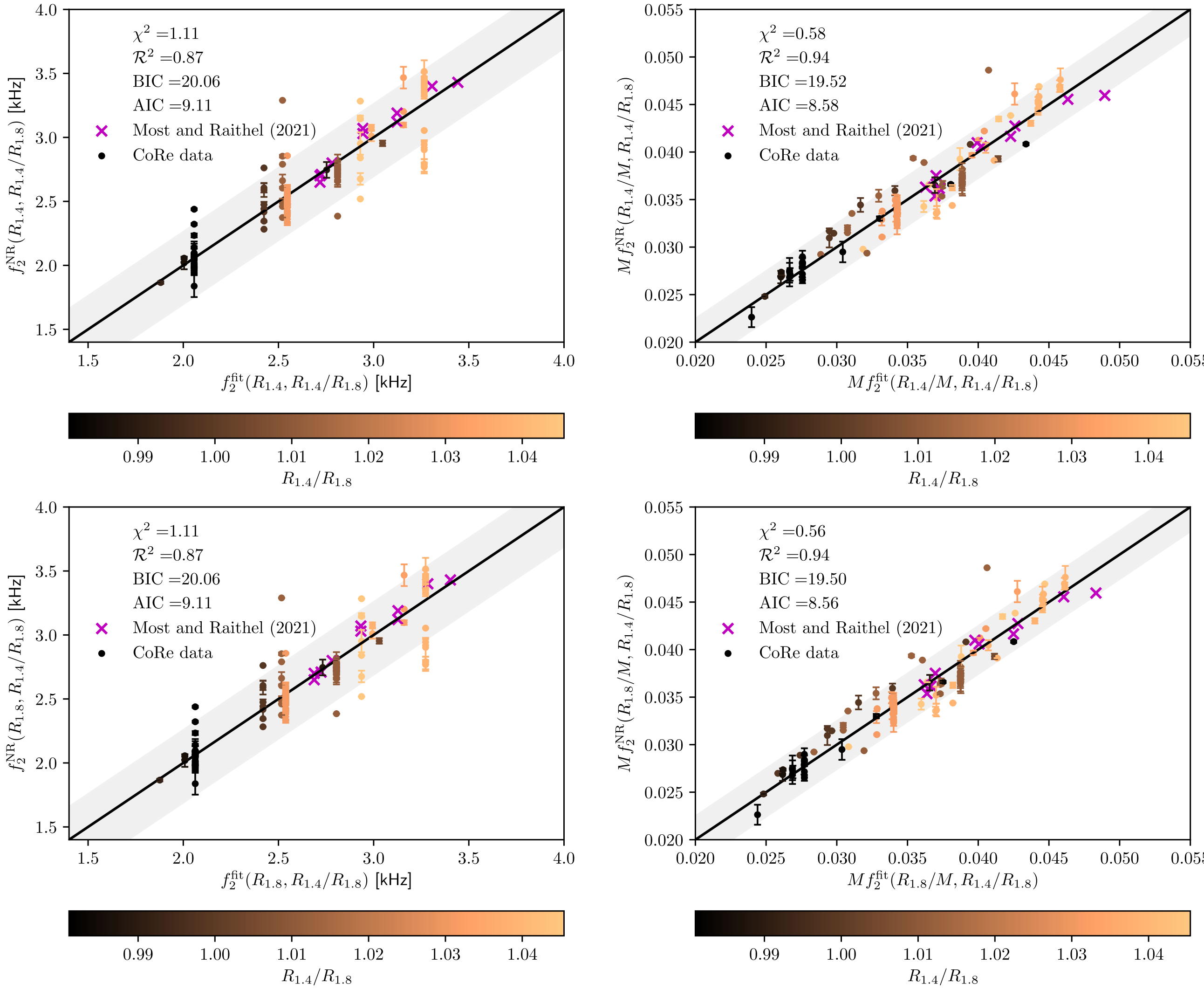

FIG. 9. Predicted values from the calibrated relations Eq. (F1) compared to the respective NR observed quantities. Top panels show $X = 1.4$ and bottom panels show $X = 1.8$. Left panels show non-mass-scaled f_2 and right panels show mass-scaled dimensionless Mf_2. The diagonal (black line) represents the case in which predictions and observations match and the gray area is the 90% credibility level. The CORE data are reported with circles colored according to $R_{1.4}/R_{1.8}$ and magenta crosses are the data extracted from [27].

values of the calibrated coefficients $\{a_i\}$ for the different quantities. Figures 8 and 9 show the NR data $f_2^{\rm NR}$ plotted against the predictions $f_2^{\rm fit}$ of the calibrated relation and the statistical quantities of interest; i.e. the χ^2 (defined in Sec. IV), the adjusted coefficient of determination $\mathcal{R}^2$, the Bayesian information criterion (BIC) and the Akaike information criterion (AIC). For the computation of the BIC and the AIC, we define a log-likelihood from Eq. (22) equal to $-\frac{1}{2}\chi^2$.

From our analysis, the calibrations performed with the mass-scaled quantities show improved trends with respect to the analogous non-mass-scaled case. This is due to the factorization of the total binary mass M, as expected by basic arguments in general relativity. Moreover, the additional contribution $R_{1.4}/R_{1.8}$ appears to be more relevant for the calibration of low-density properties, i.e. $f_2(R_{1.4})$, in agreement with [123]. However, the BIC and the AIC do not favor the introduction of these additional term, even if the χ^2 of the calibrated relation $Mf_2(R_{1.4}/M)$ slightly decreases including $R_{1.4}/R_{1.8}$ in the fit. We find that the most robust and reliable quasiuniversal relation is the mapping $Mf_2(R_{1.8}/M)$, which reinforces the hypothesis that PM quantities correlate with high-density EOS properties [17]. The differences between our results and the findings of [123] might be related to the different size and composition of the NR set, such as a different set of EOSs, or to different definitions in the statistical quantities.[10]

[10]We verified that our results are stable when employing a Gaussian likelihood or the standard Pearson's χ^2 statistic.

Notably, simulations of the CORE database show deviations comparable to the cases presented in [27,123] that cannot be fully cured with the introduction of the additional term $R_{1.4}/R_{1.8}$.

[1] S. Hild, S. Chelkowski, and A. Freise, arXiv:0810.0604.
[2] S. Hild *et al.*, Classical Quantum Gravity **28**, 094013 (2011).
[3] S. Hild, Classical Quantum Gravity **29**, 124006 (2012).
[4] M. Punturo, M. Abernathy, F. Acernese, B. Allen, N. Andersson *et al.*, Classical Quantum Gravity **27**, 194002 (2010).
[5] M. Maggiore *et al.*, J. Cosmol. Astropart. Phys. 03 (2020) 050.
[6] S. Bernuzzi, A. Nagar, T. Dietrich, and T. Damour, Phys. Rev. Lett. **114**, 161103 (2015).
[7] A. Nagar *et al.*, Phys. Rev. D **98**, 104052 (2018).
[8] S. Akcay, R. Gamba, and S. Bernuzzi, Phys. Rev. D **103**, 024014 (2021).
[9] R. Gamba, S. Bernuzzi, and A. Nagar, Phys. Rev. D **104**, 084058 (2021).
[10] S. Bernuzzi, T. Dietrich, and A. Nagar, Phys. Rev. Lett. **115**, 091101 (2015).
[11] M. Breschi, S. Bernuzzi, F. Zappa, M. Agathos, A. Perego, D. Radice, and A. Nagar, Phys. Rev. D **100**, 104029 (2019).
[12] T. Damour and A. Nagar, Phys. Rev. D **80**, 084035 (2009).
[13] T. Damour, A. Nagar, and L. Villain, Phys. Rev. D **85**, 123007 (2012).
[14] M. Agathos, F. Zappa, S. Bernuzzi, A. Perego, M. Breschi, and D. Radice, Phys. Rev. D **101**, 044006 (2020).
[15] R. Kashyap *et al.*, Phys. Rev. D **105**, 103022 (2022).
[16] A. Prakash, D. Radice, D. Logoteta, A. Perego, V. Nedora, I. Bombaci, R. Kashyap, S. Bernuzzi, and A. Endrizzi, Phys. Rev. D **104**, 083029 (2021).
[17] M. Breschi, S. Bernuzzi, D. Godzieba, A. Perego, and D. Radice, Phys. Rev. Lett. **128**, 161102 (2022).
[18] M. Breschi, A. Perego, S. Bernuzzi, W. Del Pozzo, V. Nedora, D. Radice, and D. Vescovi, Mon. Not. R. Astron. Soc. **505**, 1661 (2021).
[19] M. Breschi, R. Gamba, S. Borhanian, G. Carullo, and S. Bernuzzi, arXiv:2205.09979.
[20] M. Shibata and K. Taniguchi, Phys. Rev. D **73**, 064027 (2006).
[21] K. Hotokezaka, K. Kiuchi, K. Kyutoku, T. Muranushi, Y.-i. Sekiguchi, M. Shibata, and K. Taniguchi, Phys. Rev. D **88**, 044026 (2013).
[22] K. Takami, L. Rezzolla, and L. Baiotti, Phys. Rev. D **91**, 064001 (2015).
[23] A. Bauswein and N. Stergioulas, Phys. Rev. D **91**, 124056 (2015).
[24] F. Zappa, S. Bernuzzi, D. Radice, A. Perego, and T. Dietrich, Phys. Rev. Lett. **120**, 111101 (2018).
[25] D. Radice, S. Bernuzzi, W. Del Pozzo, L. F. Roberts, and C. D. Ott, Astrophys. J. **842**, L10 (2017).
[26] A. Bauswein, N.-U. F. Bastian, D. B. Blaschke, K. Chatziioannou, J. A. Clark, T. Fischer, and M. Oertel, Phys. Rev. Lett. **122**, 061102 (2019).
[27] E. R. Most and C. A. Raithel, Phys. Rev. D **104**, 124012 (2021).
[28] B. P. Abbott *et al.* (Virgo, KAGRA, and LIGO Scientific Collaborations), Living Rev. Relativity **21**, 3 (2018); **19**, 1 (2016).
[29] B. P. Abbott *et al.* (Virgo and LIGO Scientific Collaborations), Phys. Rev. Lett. **119**, 161101 (2017).
[30] B. P. Abbott *et al.* (Virgo and LIGO Scientific Collaborations), Astrophys. J. **851**, L16 (2017).
[31] B. P. Abbott *et al.* (LIGO Scientific and Virgo Collaborations), Astrophys. J. **875**, 160 (2019).
[32] B. P. Abbott *et al.* (LIGO Scientific and Virgo Collaborations), Phys. Rev. X **9**, 011001 (2019).
[33] M. Punturo, M. Abernathy, F. Acernese, B. Allen, N. Andersson *et al.*, Classical Quantum Gravity **27**, 084007 (2010).
[34] A. Torres-Rivas, K. Chatziioannou, A. Bauswein, and J. A. Clark, Phys. Rev. D **99**, 044014 (2019).
[35] D. Martynov *et al.*, Phys. Rev. D **99**, 102004 (2019).
[36] K. Ackley *et al.*, Pub. Astron. Soc. Aust. **37**, e047 (2020).
[37] J. A. Clark, A. Bauswein, N. Stergioulas, and D. Shoemaker, Classical Quantum Gravity **33**, 085003 (2016).
[38] K. Chatziioannou, J. A. Clark, A. Bauswein, M. Millhouse, T. B. Littenberg, and N. Cornish, Phys. Rev. D **96**, 124035 (2017).
[39] P. J. Easter, P. D. Lasky, A. R. Casey, L. Rezzolla, and K. Takami, Phys. Rev. D **100**, 043005 (2019).
[40] S. Bose, K. Chakravarti, L. Rezzolla, B. S. Sathyaprakash, and K. Takami, Phys. Rev. Lett. **120**, 031102 (2018).
[41] K. W. Tsang, T. Dietrich, and C. Van Den Broeck, Phys. Rev. D **100**, 044047 (2019).
[42] P. J. Easter, S. Ghonge, P. D. Lasky, A. R. Casey, J. A. Clark, F. H. Vivanco, and K. Chatziioannou, Phys. Rev. D **102**, 043011 (2020).
[43] T. Soultanis, A. Bauswein, and N. Stergioulas, Phys. Rev. D **105**, 043020 (2022).
[44] M. Wijngaarden, K. Chatziioannou, A. Bauswein, J. A. Clark, and N. J. Cornish, Phys. Rev. D **105**, 104019 (2022).
[45] T. Whittaker, W. E. East, S. R. Green, L. Lehner, and H. Yang, Phys. Rev. D **105**, 124021 (2022).
[46] T. Damour and A. Nagar, Phys. Rev. D **81**, 084016 (2010).
[47] M. Favata, Phys. Rev. Lett. **112**, 101101 (2014).
[48] T. Dietrich, M. Ujevic, W. Tichy, S. Bernuzzi, and B. Brügmann, Phys. Rev. D **95**, 024029 (2017).
[49] M. Shibata and K. Uryu, Prog. Theor. Phys. **107**, 265 (2002).

[50] N. Stergioulas, A. Bauswein, K. Zagkouris, and H.-T. Janka, Mon. Not. R. Astron. Soc. **418**, 427 (2011).
[51] A. Bauswein and H.-T. Janka, Phys. Rev. Lett. **108**, 011101 (2012).
[52] A. Bauswein, H. Janka, K. Hebeler, and A. Schwenk, Phys. Rev. D **86**, 063001 (2012).
[53] K. Takami, L. Rezzolla, and L. Baiotti, Phys. Rev. Lett. **113**, 091104 (2014).
[54] D. Radice, S. Bernuzzi, and C. D. Ott, Phys. Rev. D **94**, 064011 (2016).
[55] L. Lehner, S. L. Liebling, C. Palenzuela, O. L. Caballero, E. O'Connor, M. Anderson, and D. Neilsen, Classical Quantum Gravity **33**, 184002 (2016).
[56] T. Dietrich, S. Bernuzzi, M. Ujevic, and W. Tichy, Phys. Rev. D **95**, 044045 (2017).
[57] S. Bernuzzi *et al.*, Mon. Not. R. Astron. Soc. **497**, 1488 (2020).
[58] A. Perego, D. Logoteta, D. Radice, S. Bernuzzi, R. Kashyap, A. Das, S. Padamata, and A. Prakash, Phys. Rev. Lett. **129**, 032701 (2022).
[59] W. Kastaun, R. Ciolfi, A. Endrizzi, and B. Giacomazzo, Phys. Rev. D **96**, 043019 (2017).
[60] D. Radice, S. Bernuzzi, and A. Perego, Annu. Rev. Nucl. Part. Sci. **70**, 95 (2020).
[61] S. Bernuzzi, Gen. Relativ. Gravit. **52**, 108 (2020).
[62] D. Radice, A. Perego, K. Hotokezaka, S. A. Fromm, S. Bernuzzi, and L. F. Roberts, Astrophys. J. **869**, 130 (2018).
[63] K. Hotokezaka, K. Kyutoku, H. Okawa, M. Shibata, and K. Kiuchi, Phys. Rev. D **83**, 124008 (2011).
[64] A. Bauswein, T. Baumgarte, and H. T. Janka, Phys. Rev. Lett. **111**, 131101 (2013).
[65] A. Bauswein, S. Blacker, V. Vijayan, N. Stergioulas, K. Chatziioannou, J. A. Clark, N.-U. F. Bastian, D. B. Blaschke, M. Cierniak, and T. Fischer, Phys. Rev. Lett. **125**, 141103 (2020).
[66] S. Bernuzzi, D. Radice, C. D. Ott, L. F. Roberts, P. Moesta, and F. Galeazzi, Phys. Rev. D **94**, 024023 (2016).
[67] D. Radice, A. Perego, S. Bernuzzi, and B. Zhang, Mon. Not. R. Astron. Soc. **481**, 3670 (2018).
[68] M. Shibata and K. Uryu, Phys. Rev. D **61**, 064001 (2000).
[69] S. Bernuzzi, T. Dietrich, W. Tichy, and B. Brügmann, Phys. Rev. D **89**, 104021 (2014).
[70] H. Dimmelmeier, N. Stergioulas, and J. A. Font, Mon. Not. R. Astron. Soc. **368**, 1609 (2006).
[71] A. Passamonti, N. Stergioulas, and A. Nagar, Phys. Rev. D **75**, 084038 (2007).
[72] L. Baiotti, S. Bernuzzi, G. Corvino, R. De Pietri, and A. Nagar, Phys. Rev. D **79**, 024002 (2009).
[73] V. Nedora, S. Bernuzzi, D. Radice, B. Daszuta, A. Endrizzi, A. Perego, A. Prakash, M. Safarzadeh, F. Schianchi, and D. Logoteta, Astrophys. J. **906**, 98 (2021).
[74] S. Chandrasekhar, Astrophys. J. **161**, 561 (1970).
[75] J. L. Friedman and B. F. Schutz, Astrophys. J. **221**, 937 (1978).
[76] W. E. East, V. Paschalidis, F. Pretorius, and S. L. Shapiro, Phys. Rev. D **93**, 024011 (2016).
[77] S. Bernuzzi, M. Thierfelder, and B. Brügmann, Phys. Rev. D **85**, 104030 (2012).
[78] W. Kastaun, R. Ciolfi, and B. Giacomazzo, Phys. Rev. D **94**, 044060 (2016).
[79] W. Kastaun and F. Ohme, Phys. Rev. D **100**, 103023 (2019).
[80] D. Radice, S. Bernuzzi, A. Perego, and R. Haas, Mon. Not. R. Astron. Soc. **512**, 1499 (2022).
[81] S. Bernuzzi, A. Nagar, and R. De Pietri, Phys. Rev. D **77**, 044042 (2008).
[82] E. Berti, V. Cardoso, and A. O. Starinets, Classical Quantum Gravity **26**, 163001 (2009).
[83] E. Berti and A. Klein, Phys. Rev. D **90**, 064012 (2014).
[84] J. Calderón Bustillo, S. H. W. Leong, T. Dietrich, and P. D. Lasky, Astrophys. J. Lett. **912**, L10 (2021).
[85] T. Dietrich, S. Bernuzzi, B. Brügmann, and W. Tichy, in *2018 26th Euromicro International Conference on Parallel, Distributed and Network-based Processing (PDP)* (2018), pp. 682–689, arXiv:1803.07965.
[86] S. Bernuzzi and T. Dietrich, Phys. Rev. D **94**, 064062 (2016).
[87] Y. Fujimoto, K. Fukushima, K. Hotokezaka, and K. Kyutoku, Phys. Rev. Lett. **130**, 091404 (2023).
[88] T. Dietrich, D. Radice, S. Bernuzzi, F. Zappa, A. Perego, B. Brügmann, S. V. Chaurasia, R. Dudi, W. Tichy, and M. Ujevic, Classical Quantum Gravity **35**, 24LT01 (2018).
[89] http://www.computational-relativity.org/, Computational Relativity.
[90] K. Kawaguchi, K. Kiuchi, K. Kyutoku, Y. Sekiguchi, M. Shibata, and K. Taniguchi, Phys. Rev. D **97**, 044044 (2018).
[91] K. Kiuchi, K. Kawaguchi, K. Kyutoku, Y. Sekiguchi, M. Shibata, and K. Taniguchi, Phys. Rev. D **96**, 084060 (2017).
[92] K. Kiuchi, K. Kyohei, K. Kyutoku, Y. Sekiguchi, and M. Shibata, Phys. Rev. D **101**, 084006 (2020).
[93] A. Camilletti, L. Chiesa, G. Ricigliano, A. Perego, L. C. Lippold, S. Padamata, S. Bernuzzi, D. Radice, D. Logoteta, and F. M. Guercilena, Mon. Not. R. Astron. Soc. **516**, 4760 (2022).
[94] B. Brügmann, J. A. Gonzalez, M. Hannam, S. Husa, U. Sperhake, and W. Tichy, Phys. Rev. D **77**, 024027 (2008).
[95] M. Thierfelder, S. Bernuzzi, and B. Brügmann, Phys. Rev. D **84**, 044012 (2011).
[96] D. Radice and L. Rezzolla, Astron. Astrophys. **547**, A26 (2012).
[97] S. Banik, M. Hempel, and D. Bandyopadhyay, Astrophys. J. Suppl. Ser. **214**, 22 (2014).
[98] I. Bombaci and D. Logoteta, Astron. Astrophys. **609**, A128 (2018).
[99] D. Logoteta, A. Perego, and I. Bombaci, Astron. Astrophys. **646**, A55 (2021).
[100] S. Typel, G. Ropke, T. Klahn, D. Blaschke, and H. H. Wolter, Phys. Rev. C **81**, 015803 (2010).
[101] M. Hempel, T. Fischer, J. Schaffner-Bielich, and M. Liebendorfer, Astrophys. J. **748**, 70 (2012).
[102] J. M. Lattimer and F. D. Swesty, Nucl. Phys. **A535**, 331 (1991).
[103] A. W. Steiner, J. M. Lattimer, and E. F. Brown, Astrophys. J. **765**, L5 (2013).
[104] A. S. Schneider, L. F. Roberts, and C. D. Ott, Phys. Rev. C **96**, 065802 (2017).
[105] M. Alford, M. Braby, M. W. Paris, and S. Reddy, Astrophys. J. **629**, 969 (2005).

[106] L. Engvik, G. Bao, M. Hjorth-Jensen, E. Osnes, and E. Ostgaard, Astrophys. J. **469**, 794 (1996).
[107] H. Müther, M. Prakash, and T. L. Ainsworth, Phys. Lett. B **199**, 469 (1987).
[108] H. Müller and B. D. Serot, Nucl. Phys. **A606**, 508 (1996).
[109] F. Douchin and P. Haensel, Astron. Astrophys. **380**, 151 (2001).
[110] B. D. Lackey, M. Nayyar, and B. J. Owen, Phys. Rev. D **73**, 024021 (2006).
[111] J. S. Read, B. D. Lackey, B. J. Owen, and J. L. Friedman, Phys. Rev. D **79**, 124032 (2009).
[112] A. Nagar, G. Pratten, G. Riemenschneider, and R. Gamba, Phys. Rev. D **101**, 024041 (2020).
[113] S. Bernuzzi, A. Nagar, S. Balmelli, T. Dietrich, and M. Ujevic, Phys. Rev. Lett. **112**, 201101 (2014).
[114] F. Zappa, S. Bernuzzi, F. Pannarale, M. Mapelli, and N. Giacobbo, Phys. Rev. Lett. **123**, 041102 (2019).
[115] D. Radice, Astrophys. J. **838**, L2 (2017).
[116] S. Vitale, W. Del Pozzo, T. G. Li, C. Van Den Broeck, I. Mandel, B. Aylott, and J. Veitch, Phys. Rev. D **85**, 064034 (2012).
[117] R. Storn and K. Price, J. Global Optim. **11**, 341 (1997).
[118] T. Damour, A. Nagar, and M. Trias, Phys. Rev. D **83**, 024006 (2011).
[119] K. Chatziioannou, A. Klein, N. Yunes, and N. Cornish, Phys. Rev. D **95**, 104004 (2017).
[120] R. Gamba, M. Breschi, S. Bernuzzi, M. Agathos, and A. Nagar, Phys. Rev. D **103**, 124015 (2021).
[121] M. Breschi, R. Gamba, and S. Bernuzzi, Phys. Rev. D **104**, 042001 (2021).
[122] A. Vijaykumar, S. J. Kapadia, and P. Ajith, Mon. Not. R. Astron. Soc. **513**, 3577 (2022).
[123] C. A. Raithel and E. R. Most, Astrophys. J. Lett. **933**, L39 (2022).
[124] Y. Sekiguchi, K. Kiuchi, K. Kyutoku, and M. Shibata, Phys. Rev. Lett. **107**, 211101 (2011).
[125] Y.-J. Huang, L. Baiotti, T. Kojo, K. Takami, H. Sotani, H. Togashi, T. Hatsuda, S. Nagataki, and Y.-Z. Fan, Phys. Rev. Lett. **129**, 181101 (2022).
[126] K. Chatziioannou and S. Han, Phys. Rev. D **101**, 044019 (2020).
[127] E. R. Most, L. Jens Papenfort, V. Dexheimer, M. Hanauske, H. Stoecker, and L. Rezzolla, Eur. Phys. J. A **56**, 59 (2020).
[128] https://github.com/matteobreschi/bajes.
[129] D. Radice, F. Galeazzi, J. Lippuner, L. F. Roberts, C. D. Ott, and L. Rezzolla, Mon. Not. R. Astron. Soc. **460**, 3255 (2016).
[130] K. Kiuchi, K. Kyutoku, Y. Sekiguchi, and M. Shibata, Phys. Rev. D **97**, 124039 (2018).